



Sarakinos, S. and Busse, A. (2022) Investigation of rough-wall turbulence over barnacle roughness with increasing solidity using direct numerical simulations. *Physical Review Fluids*, 7(6), 064602. (doi: [10.1103/PhysRevFluids.7.064602](https://doi.org/10.1103/PhysRevFluids.7.064602)).

This is the Author Accepted Manuscript.

There may be differences between this version and the published version. You are advised to consult the publisher's version if you wish to cite from it.

<http://eprints.gla.ac.uk/26988/>

Deposited on: 29 April 2022

Enlighten – Research publications by members of the University of Glasgow  
<http://eprints.gla.ac.uk>

1 **Investigation of rough-wall turbulence over barnacle roughness with increasing**  
2 **solidity using direct numerical simulations**

3 Sotirios Sarakinos\* and Angela Busse†  
4 *James Watt School of Engineering*  
5 *University of Glasgow*  
6 *Glasgow, G12 8QQ*  
7 (Dated: April 27, 2022)

Barnacle-type roughness can be considered as a hybrid-form of roughness that combines some of the topographical features of traditional regular rough surfaces composed of discrete roughness elements of uniform size and shape, and of irregular rough surfaces that exhibit features with a wide distribution of sizes and shapes, covering the surface with a random areal distribution. In this study, the influence of barnacle-type rough surfaces with increasing coverage on wall-bounded turbulence is investigated using direct numerical simulations of turbulent channel flow. The barnacle-type rough surfaces were generated with an algorithm that mimics the settlement behaviour of barnacles, and the set of seven different surfaces describe the evolution of barnacle fouling with increasing coverage ranging from a lightly fouled surface with small isolated barnacle clusters (10% coverage) to a surface that is fully covered by barnacles (85% coverage). The roughness function recovers the expected trend with frontal solidity, attaining its maximum at a frontal solidity of approximately 0.2. Mean flow, Reynolds stress, and dispersive stresses show signatures of the clustering of roughness features, i.e., the barnacle colonies, at low coverage. This is most distinct for the streamwise Reynolds stresses where a double peak is observed at the lowest coverage; the inner peak can be interpreted as a partial recovery of smooth-wall behaviour over the large connected unfouled sections of this surface. The flow over the rough surfaces is further investigated by a topographical characterisation of the blanketing layer, i.e., the effective shape of the rough surface ‘perceived’ by the outer flow. A linear relationship between the roughness function and the effective slope of the blanketing layer is observed.

---

\* Sotirios.Sarakinos@glasgow.ac.uk

† Angela.Busse@glasgow.ac.uk

## I. INTRODUCTION

The accumulation of marine organisms on surfaces submerged in sea water is collectively termed marine biofouling [1]. Its negative effect on the performance of sea-faring vessels has been known since ancient times, while the use of coatings as antifoulants has been recorded since the early 17th century [2]. The use of poisonous chemicals in antifoulants, such as dichlorodiphenyltrichloroethane (DDT) and arsenic, led to their ban in the 1960s and their replacement by tributyltin (TBT) based coatings [3]. However, TBT's negative effects on the environment were also severe, leading to the reduction of its use in antifoulants during the 1980s and 1990s, and finally to its international ban in 2008 [4]. This ban has led to increased interest in the investigation of marine biofouling and its negative effects on marine vehicles and man-made structures.

Marine biofouling is primarily categorized into microfouling and macrofouling. The former includes bacteria sized organisms and inorganic matter in particulate form that compose a thin film of slime, termed biofilm [2]. The latter includes all types of biofouling organisms visible to the naked eye, such as sea-squirts (*Ascidacea*), sea-mats (*Bryozoa*), hydroids (*Hydrozoa*), mussels (*Bivalvia*), tube-worms (*Serpulidae*), and barnacles (*Cirripedia*) [5]. Both microfouling and macrofouling have been found to increase frictional resistance of substrate surfaces [6 and 7], however the effect caused by calcareous macrofouling is considered to be the most severe [8–10], and sessile barnacles (*Sessilia*) are some of the most dominant biofouling species [11].

The main harmful effect of marine biofouling is the increased roughness of underwater surfaces, where the biofouling organisms settle, resulting in a decrease of vehicle speed, and increased power requirements [12]. Biofouling can also affect propellers and the blades of wave and tidal turbines, reducing their efficiency by increasing their effective diameters, leading to increased drag and inertia loads [13–15]. Further adverse effects linked to the accumulation of marine organisms on surfaces are the destruction of coatings and increased corrosion. The significant economic impact of biofouling can be illustrated by a practical example given by Schultz *et al.* [16] who estimated that the fuel consumption of a US Navy Arleigh-Burke-class destroyer increases by 20.4% at a fouling rating (FR) of 60, which corresponds to a surface affected by small calcareous fouling or weeds.

The increase in frictional resistance of submerged surfaces due to calcareous marine biofouling has been studied both through experimental investigations and numerical simulations of the flow over representative rough surfaces [7, 17–19]. For example, Schultz [8] performed towing tank experiments to investigate the drag resistance of metal test plates with different coatings that were exposed to a biofouling environment for over nine months. The experiments showed that while in an unfouled state all plates performed similarly, for the fouled plates the Hama roughness function  $\Delta U^+$  [20] increased with increasing coverage by biofouling. Monty *et al.* [10] investigated the flow over a sparsely biofouled surface with light calcareous tube-worm fouling using wind tunnel experiments. The surface was obtained from a 3D-scan of a plate that had been exposed for two months to a biofouling environment. Compared to the experiments by Schultz, the equivalent sand grain roughness of their surface was found to be similar to that of heavy biofilm coatings, but lower than the lightly fouled cases investigated by Schultz [8].

The process of obtaining real marine biofouling specimens can be time-consuming and costly, since the test plates have to be exposed to sea-water conditions for several months to accumulate organisms, and it is difficult to exactly control the type and amount of settling organisms. Therefore, artificially created forms of marine roughness are also used for the investigation of the fluid dynamic effects biofouling [9, 18, 21, 22] where typically barnacle-shaped roughness elements of uniform size are placed in regular or staggered arrangements to create rough surfaces with well-controlled roughness height, surface coverage, and frontal solidity. However, natural barnacle-fouled surfaces exhibit neither a perfectly uniform height distribution due to natural variations in barnacle size nor a perfectly regular arrangement of the barnacles, since barnacles tend to settle next to each other and form colonies. These properties are also exhibited by other forms of roughness with discrete features, e.g., urban roughness is often formed of buildings of various heights that are distributed in a non-uniform pattern, and surface pitting corrosion typically originates from localized sites which subsequently grow to affect the surrounding surface area [23].

Barnacle-type roughness, and similar types of rough surfaces with randomly sized roughness features in non-uniform clustered arrangements, can be considered hybrid forms of roughness that fall into the range between the widely studied artificial regular rough surfaces formed of regular arrangements of uniformly sized roughness elements, such as cubes or hemispheres (see e.g. [24–28]), and general irregular forms of roughness with a uniformly random spatial distribution of roughness features (see e.g. [29–36]). The investigation of realistic barnacle-type roughness is therefore not only of interest in the context of marine biofouling, but can also serve as an useful example for a class of roughness that falls into the spectrum between discrete versus distributed, and regular versus irregular forms of roughness that have been the focus of most previous investigations of the topography-dependence of rough wall turbulence.

In the current study, the effect of a set of barnacle-type rough surfaces with increasing coverage on wall-bounded turbulence is investigated using direct numerical simulations. All surfaces have been created with an algorithm that mimics the gregarious behaviour of barnacles resulting in rough surfaces, with clustered features composed of barnacle-shape roughness elements with a realistic distribution of sizes (see section II A). Direct numerical simulations

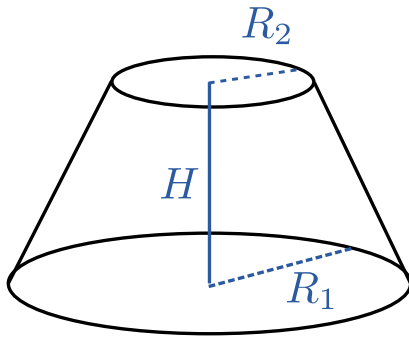


FIG. 1: Representation of the barnacle geometry as a conical frustum following Sadique [22].  $H$ : barnacle height,  $R_1$ : base radius, and  $R_2$ : upper radius.

65 of turbulent channel flow at  $Re_\tau = 395$  were used to obtain mean flow and turbulence statistics for each surface (section  
 66 II B). Results for the roughness function are discussed in relation to frontal solidity and effective slope in section III A.  
 67 Mean flow, Reynolds, and dispersive stress statistics are discussed in sections III B and III C. A detailed investigation  
 68 of the mean flow field in the vicinity of the rough surfaces (see sections III D and III E) shows that the increase  
 69 and subsequent drop in fluid dynamic roughness effect with increasing coverage can be related to changes in the  
 70 flow patterns within the rough surfaces and the topography of the blanketing layer that forms above the roughness.  
 71 Conclusions are given in section IV.

## 72 II. METHODOLOGY

73 The aim of the current study is to investigate the dependence of the roughness function and the statistical properties  
 74 of the near-wall flow on the degree of coverage by barnacles, a typical form of calcareous macro-fouling encountered  
 75 in marine environments. Surface coverage is known to be a key parameter in the context of marine biofouling [8].  
 76 Seven different rough surfaces were generated with an algorithm that mimics the settlement behaviour of barnacles.  
 77 For each surface, a direct numerical simulation of rough-wall turbulent channel flow was conducted to obtain its effect  
 78 on the mean flow and turbulence properties.

### 79 A. The surfaces

80 Barnacles are a species of arthropods that belong to the taxon of *Crustacea*. The order *Sessilia*[2], commonly  
 81 known as acorn barnacles or sessile barnacles [37], is the most typical form found in marine biofouling. The acorn  
 82 barnacle settlement behaviour has been well documented [38–42]. Most researchers agree that acorn barnacles prefer  
 83 to form colonies and settle in places where mature barnacles of the same species have already settled [38 and 39].  
 84 In the current study, rough surfaces were generated with an algorithm that mimics this gregarious behaviour of  
 85 barnacles [43]. Barnacles are modelled as conical frustra (see figure 1) following the approach by Sadique [22], and  
 86 a realistic distribution of barnacle shapes and sizes is used (see table I). Starting from a set of seed barnacles,  
 87 additional barnacle shapes are placed successively on a flat surface in the vicinity of other already settled barnacles,  
 88 mimicking their tendency to form colonies (see figure 2 (a)). By gradual addition of further barnacles the coverage  
 89 of the surfaces is increased (see figure 2 parts (b) to (f)) until no further barnacles can be placed and the maximum  
 90 coverage is attained (see figure 2 (g)).

93 In total, seven surfaces were generated at 10%, 15%, 30%, 45%, 60%, 75%, and 85% coverage. Each coverage state  
 94 is derived from the previous one by adding more barnacles in order to achieve the desired coverage percentage, thus  
 95 realizing the evolution of a barnacle colony.

96 The size of the original surface was  $250\text{mm} \times 125\text{mm}$  and the barnacles' geometric characteristics were based on the  
 97 ranges given by Sadique [22].  $AR$  denotes the aspect ratio of the barnacle, defined as the ratio of height  $H$  over base  
 98 diameter  $2R_1$ , and  $RR$  is the ratio of the upper radius  $R_2$  to the base radius  $R_1$  (see Table I). To maintain a constant  
 99 reference roughness height for all the surfaces, the geometry of the first barnacle was defined with the maximum value  
 100 for  $H$ .

102 The topographical properties of all rough surfaces are presented in Table II. For the direct numerical simulations  
 103 all surfaces were non-dimensionalised based on the mean channel half-height  $\delta$ . The streamwise extent of the flow

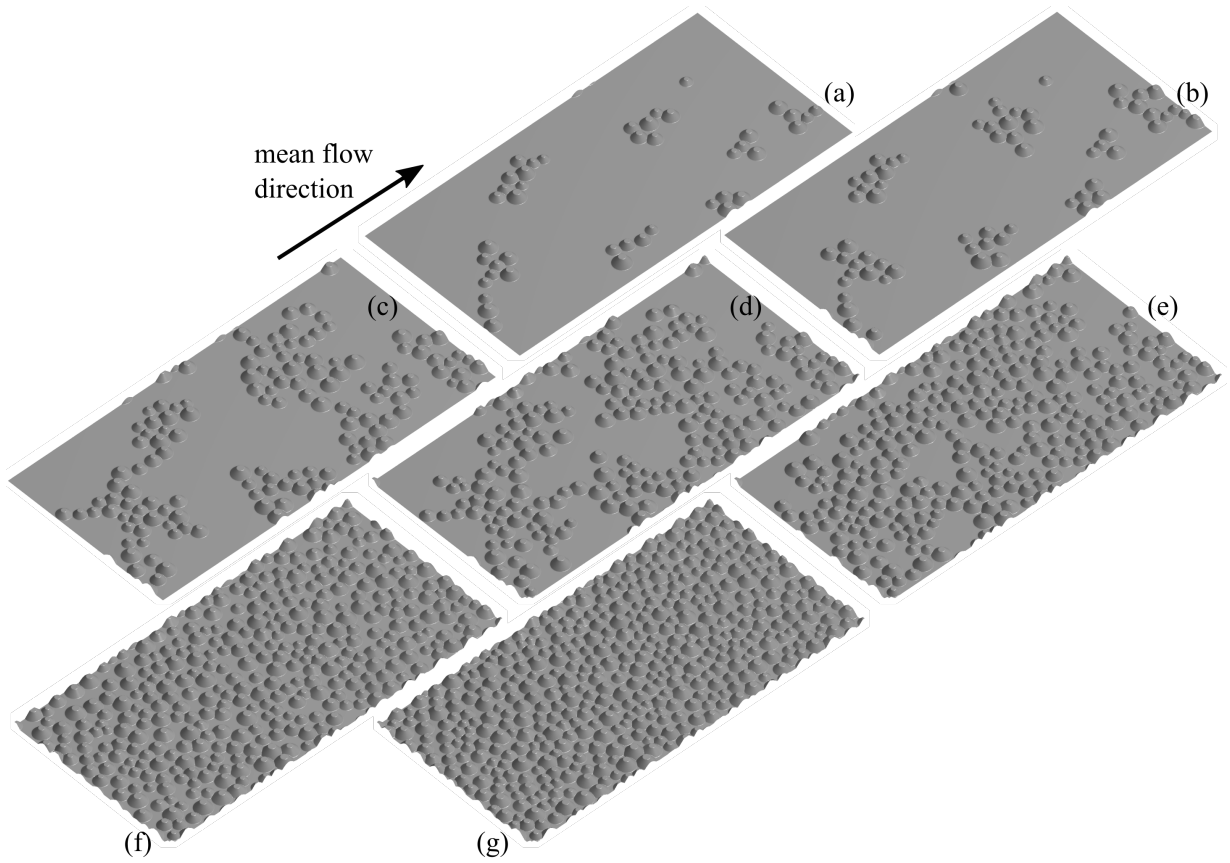


FIG. 2: Visualisation of all rough surfaces in order of increasing coverage by barnacles: (a) 10% coverage; (b) 15% coverage; (c) 30% coverage; (d) 45% coverage; (e) 60% coverage; (f) 75% coverage; (g) 85% coverage

TABLE I: Geometric properties of the barnacles used to generate the rough surfaces:  $R_1$  - base radius;  $RR$  - ratio of upper to lower radius;  $AR$  - aspect ratio.

	$R_1$ (mm)	$R_1/\delta$	$RR$	$AR$
minimum	3.5	0.0880	0.31	0.34
maximum	6	0.1508	0.4	0.42

TABLE II: Topographical parameters of the barnacle surfaces.  $N_b$ : number of barnacles;  $\lambda_f$ : frontal solidity;  $ES$ : effective slope,  $S_{z,max}$ : maximum peak-to-valley height;  $S_a$ : mean roughness height;  $S_q$ : rms roughness height;  $S_{sk}$ : Skewness;  $S_{ku}$ : Kurtosis;  $L_{corr}^x$ : streamwise correlation length;  $L_{corr}^y$ : spanwise correlation length;  $z_0$ : smooth-wall displacement.

Coverage	$N_b$	$\lambda_f$	$ES$	$S_a/\delta$	$S_q/\delta$	$S_{sk}$	$S_{ku}$	$L_{corr}^x/\delta$	$L_{corr}^y/\delta$	$z_0/\delta$	linestyle
10 %	44	0.033	0.067	0.0089	0.0180	4.06	19.5	0.26	0.19	-0.0049	—
15 %	66	0.050	0.099	0.0126	0.0214	3.16	12.4	0.28	0.31	-0.0074	- - - -
30 %	135	0.102	0.204	0.0219	0.0289	1.87	5.36	0.16	0.23	-0.0153	.....
45 %	202	0.146	0.294	0.0265	0.0321	1.31	3.48	0.13	0.13	-0.0219	- . - .
60 %	275	0.198	0.397	0.0292	0.0341	0.88	2.52	0.11	0.11	-0.0296	—
75 %	345	0.245	0.489	0.0295	0.0343	0.58	2.15	0.095	0.095	-0.0367	- - - -
85 %	440	0.276	0.553	0.0277	0.0326	0.40	2.11	0.087	0.087	-0.0421	.....

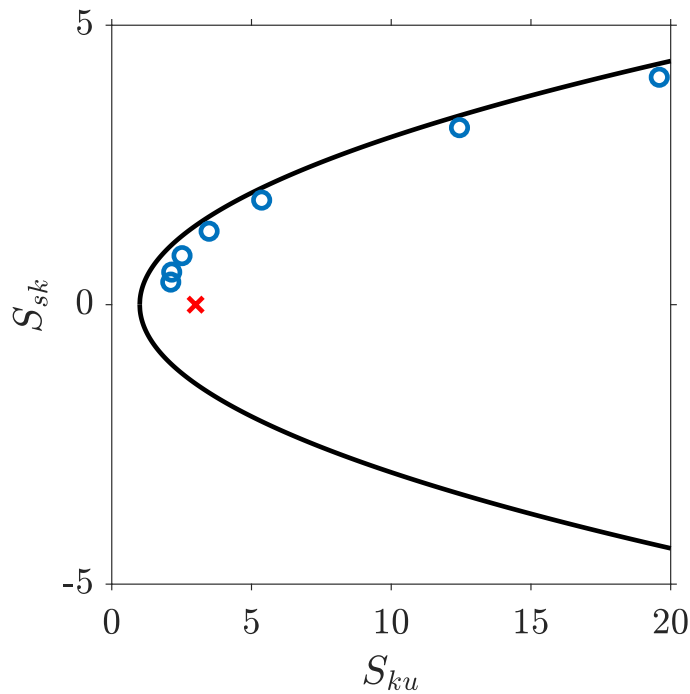


FIG. 3: Skewness plotted versus kurtosis of barnacle covered surface roughness (blue circles). The solid line marks the boundary of Pearson's inequality  $S_{ku} = S_{sk}^2 + 1$ ; the red cross indicates the values for a Gaussian height distribution ( $S_{sk} = 0$ ,  $S_{ku} = 3$ ).

104 domain  $\ell_x$  was set to  $2\pi\delta$ , with the spanwise extent  $\ell_y = \pi\delta$ . This yields a maximum peak-to-valley height of  $S_{z,max}$   
 105 of  $0.1267\delta$  for all surfaces. This is essentially the height of the first barnacle added on the surface and will be used  
 106 as a reference roughness height in the following. The height of the smallest barnacle in the population varies slightly  
 107 due to the random nature of the surfaces dropping from  $0.0684\delta$  for the 10% surface to  $0.0603\delta$  for the 85% surface.  
 108 In the following, the latter will be referred to as 'minimum barnacle height'.

109 The topographical parameters change with increasing coverage (see Table II), most notably skewness and kurtosis  
 110 of the roughness height distribution (see Fig. 3). The solid line in Figure 3 represents the lower bound for kurtosis  
 111 based on Pearson's inequality [44]:

$$S_{ku} \geq S_{sk}^2 + 1 \quad (1)$$

112 For low coverage states, skewness and kurtosis acquire high values due to the sparseness of the roughness elements  
 113 and the corresponding  $(S_{sk}, S_{ku})$  points on the skewness-kurtosis map fall close to the outer boundary imposed by  
 114 Pearson's inequality. Since the roughness elements are tapering and the roughness elements have a distribution of  
 115 heights, the  $(S_{sk}, S_{ku})$  points however do not coincide with the inequality's boundary, since this would require height  
 116 distributions that are Bernoulli distributions, as found for surfaces constructed using non-tapering roughness elements  
 117 of uniform height such as cubes or cylindrical posts. With increasing surface coverage, skewness and kurtosis reduce;  
 118 the skewness remains positive for all surfaces, but the kurtosis drops below 3 for the densely populated surfaces, i.e.,  
 119 negative excess kurtosis values are attained at coverage of 60% and above.

120 In the context of empirical roughness correlation the frontal solidity  $\lambda_f$  and effective slope  $ES = 2\lambda_f$  values are also  
 121 of particular interest [45, 46]. These naturally increase with the placement of more barnacle shapes on the smooth  
 122 reference surface. The correlation between the effect of roughness on fluid flows and  $\lambda_f$  and  $ES$  is discussed in section  
 123 III A. [Womack et al. \[47\] found for uniform random distributions of roughness elements that the exact placement of](#)  
 124 [roughness features has negligible influence on the roughness effect.](#)

125

## B. Direct numerical simulations

126 The embedded boundary method code iIMB [48] was used for the direct numerical simulation of turbulent channel  
 127 flow over the rough surfaces. The code employs second-order central differences on a staggered grid to evaluate the  
 128 spatial derivatives of the incompressible Navier-Stokes equations and a second-order Adams-Bashforth method for the

TABLE III: Grid and domain sizes used for the rough and the smooth wall simulations.  $\ell_x$ : domain size in streamwise direction;  $\ell_y$ : domain size in spanwise direction;  $N_x, N_y, N_z$ : number of grid-points in streamwise, spanwise, and wall-normal direction;  $\Delta x^+, \Delta y^+$  uniform grid spacing in the streamwise and spanwise direction;  $\Delta z_{min}^+$ : minimum wall-normal grid-spacing;  $\Delta z_{max}^+$ : maximum wall-normal grid spacing.

type	$\ell_x/\delta$	$\ell_y/\delta$	$N_x$	$N_y$	$N_z$	$\Delta x^+$	$\Delta y^+$	$\Delta z_{min}^+$	$\Delta z_{max}^+$
rough	$2\pi$	$\pi$	864	432	512	2.87	2.87	0.67	$\leq 3.98$
smooth	8	4	640	320	360	4.94	4.94	0.50	3.98

temporal discretisation. The rough walls are resolved with an iterative version of the embedded boundary method by Yang and Balaras [49], a non-boundary-conforming method for simulating turbulent flows over complex boundaries on Cartesian grids.

Periodic boundary conditions are employed in the streamwise and spanwise direction. The rough-wall boundary conditions are applied to both the upper and the lower channel wall, with the rough surface at the upper wall shifted by half the domain size in the spanwise and streamwise direction to minimise local blockage effects. By applying a small offset  $z_0$  to the smooth wall plane on which the barnacles are settled, the mean roughness height of each surface is set to zero, thus defining the wall-normal coordinate  $z = 0$  at the location of the roughness mean plane for each simulation, which is consistent with the approach used in several previous studies on topography-dependence of rough-wall turbulence [32, 48, 50, 51].

The simulation parameters are summarized in Table III. The parameters for the smooth-wall reference case are also given in Table III. Uniform and dense grid spacing is employed in the streamwise ( $x$ -) and spanwise ( $y$ -) directions in all rough-wall cases to resolve the complex geometries of the irregular barnacle surfaces. In the wall-normal ( $z$ -) direction uniform spacing  $\Delta z_{min}^+$  is used within the roughness layer, i.e., in the range between the smooth settling plane and the highest barnacle height, and the grid is gradually stretched above attaining a maximum spacing of  $\Delta z_{max}^+$  at the channel centre. All simulations were performed at the same friction Reynolds number  $Re_\tau = 395$  with a constant mean streamwise pressure gradient. Time averages were taken over at minimum of 70 flow-through times ( $\ell_x/U_b$ ) under fully developed flow conditions. All mean flow, Reynolds, and dispersive profiles presented in the following are obtained using intrinsic averaging, i.e. averages are taken over the fluid-occupied areas.

### III. MEAN FLOW STATISTICS

In this section the roughness function's dependency on the frontal solidity and effective slope is presented (see subsection III A), followed by a discussion of the mean velocity profile in subsection III B, and the Reynolds and dispersive stress profiles in subsection III C. In last two subsections, the structure of the time average flow field within and in the vicinity of the rough surfaces will be discussed based on the probability density functions of the local time-averaged streamwise velocity (see subsection III D) and the statistics of the blanketing layer that forms over the rough surface (see subsection III E).

#### A. Roughness function

The Hama roughness function  $\Delta U^+$  is defined as the downward shift in mean streamwise velocity profile for a rough wall compared to the smooth wall equivalent at the same friction Reynolds number [20]. In the current study,  $\Delta U^+$  was computed by subtracting the centreline velocity values of the rough-wall cases from the smooth-wall reference case consistent with the approach used in [32, 36, 51] since an excellent collapse was observed for the velocity defect profile above the roughness layer (see figure 6 (b)). The roughness function values, the centreline velocity, and the bulk velocity values are presented in Table IV. The roughness function values for the 10% and 15% cases fall into the upper transitionally rough region, whereas the higher coverage states can be considered fully rough based on their  $\Delta U^+$  values.

Figure 4 (a) shows the roughness function as a function of frontal solidity  $\lambda_f$ . With the increase in surface coverage and thus frontal solidity,  $\Delta U^+$  is increasing, attaining its maximum at 60% coverage and a frontal solidity value of approximately 0.2. Beyond this point  $\Delta U^+$  is decreasing for the surfaces at 75% and 85% coverage. The increase of the roughness function values for low coverage can be attributed to the increase of the number of roughness elements on the surface. For high coverage, sheltering effects become of increasing importance, which can explain the decreasing trend that is observed for coverage above 60%. For comparison, roughness function values from MacDonald *et al.*

TABLE IV: Centreline velocity, bulk flow velocity and roughness function value for all surfaces at  $Re_\tau = 395$ . Estimates for the equivalent sand-grain roughness  $k_s^{est}$  were obtained from the  $\Delta U^+$  values using the approach described in Chung *et al.* [46].

% Coverage	$U_c/u_\tau$	$U_b/u_\tau$	$\Delta U^+$	$k_s^{est}/S_{z,max}$
10	15.42	12.84	4.87	0.57
15	14.21	11.68	6.09	0.92
30	12.96	10.44	7.33	1.52
45	12.57	10.04	7.72	1.77
60	12.40	9.82	7.89	1.90
75	12.81	10.07	7.48	1.61
85	13.22	10.51	7.08	1.37

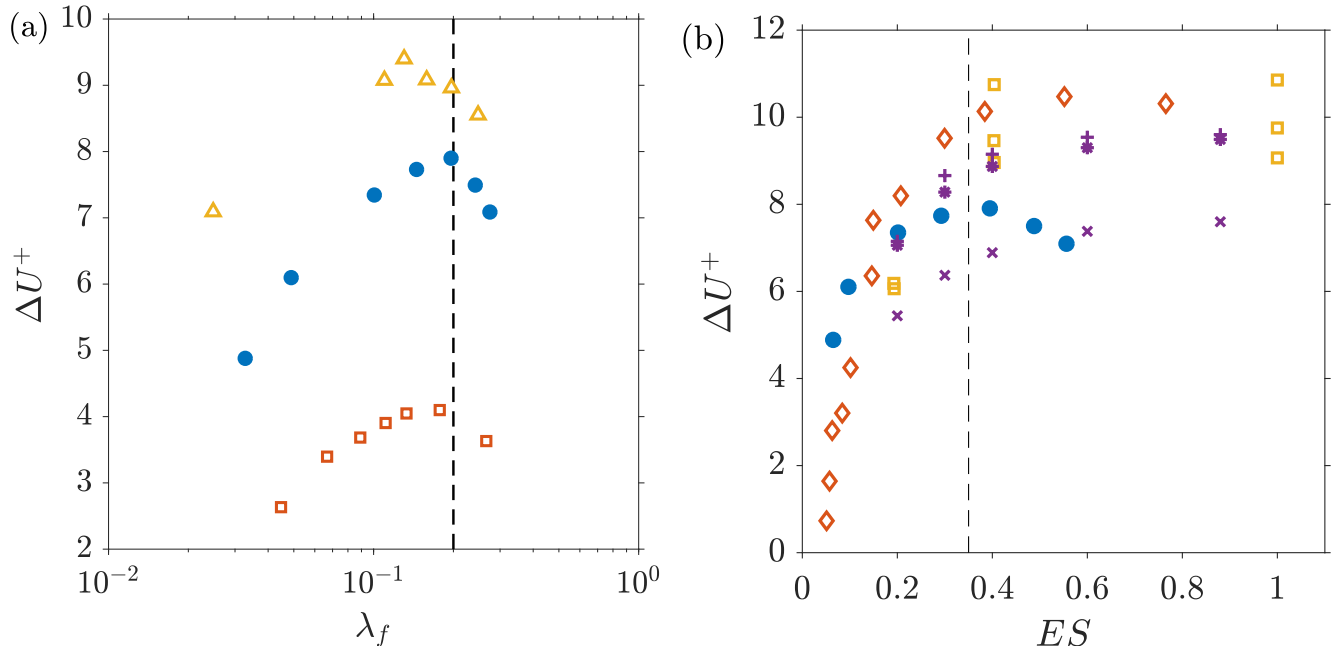


FIG. 4: (a) Roughness function  $\Delta U^+$  against surface frontal solidity  $\lambda_f$  (blue filled circles); Data by MacDonald *et al.* [52] (orange squares) and Leonardi and Castro [26] (yellow triangles) is shown for comparison. (b)  $\Delta U^+$  against surface effective slope  $ES$  (blue filled circles). Data by Napoli *et al.* [45] (orange diamonds), Schultz and Flack [53] (yellow squares), and Forooghi *et al.* [33] (purple symbols, +:  $S_{sk} \approx 0.2$ , \*:  $S_{sk} \approx 0.67$ , x:  $S_{sk} = -0.33$ ) is shown for comparison.

171 [52] for regular sinusoidal egg-carton roughness and from Leonardi and Castro [26] for regular cube roughness are  
 172 also shown in Figure 4. The overall behaviour of the roughness function with respect to the surface frontal solidity is  
 173 similar, although the peak is found at different  $\lambda_f$  values.

174 A similar dependence of the roughness effect on solidity has been observed in a number of other studies. Jiménez  
 175 [54] collated results from the experiments by [24], Webb *et al.* [55], Tani [56], and Bandyopadhyay [57] and found that  
 176 the maximum value of the roughness function was attained at  $\lambda_f \approx 0.15$  in most cases. More recently, MacDonald  
 177 *et al.* [52] suggested that the critical frontal solidity value is in the region  $0.15 \leq \lambda_f \leq 0.2$ , based on their own results  
 178 that placed the maximum at 0.18 and on the results by Placidi and Ganapathisubramani [58] who found a maximum  
 179 bulk drag at  $\lambda_f = 0.21$ . The maximum location for the barnacle surfaces at  $\lambda_f \approx 0.2$  therefore falls within the  
 180 expected range.

181 As discussed above, frontal solidity and effective slope of a surface are directly related. In Figure 4 (b) the results  
 182 from the barnacle covered surfaces are compared to those by Napoli *et al.* [45], Schultz and Flack [53], and Forooghi  
 183 *et al.* [33], who performed simulations or experiments over rough surfaces with increasing effective slope. Napoli  
 184 *et al.* [45] performed simulations over 2D wavy rough surfaces generated by superposition of sinusoidal functions  
 185 with random amplitude which had no dependency on the spanwise direction. Their surfaces show an increase in  
 186 the effective slope, but based on their definition, maintain approximately zero skewness. Schultz and Flack [53]

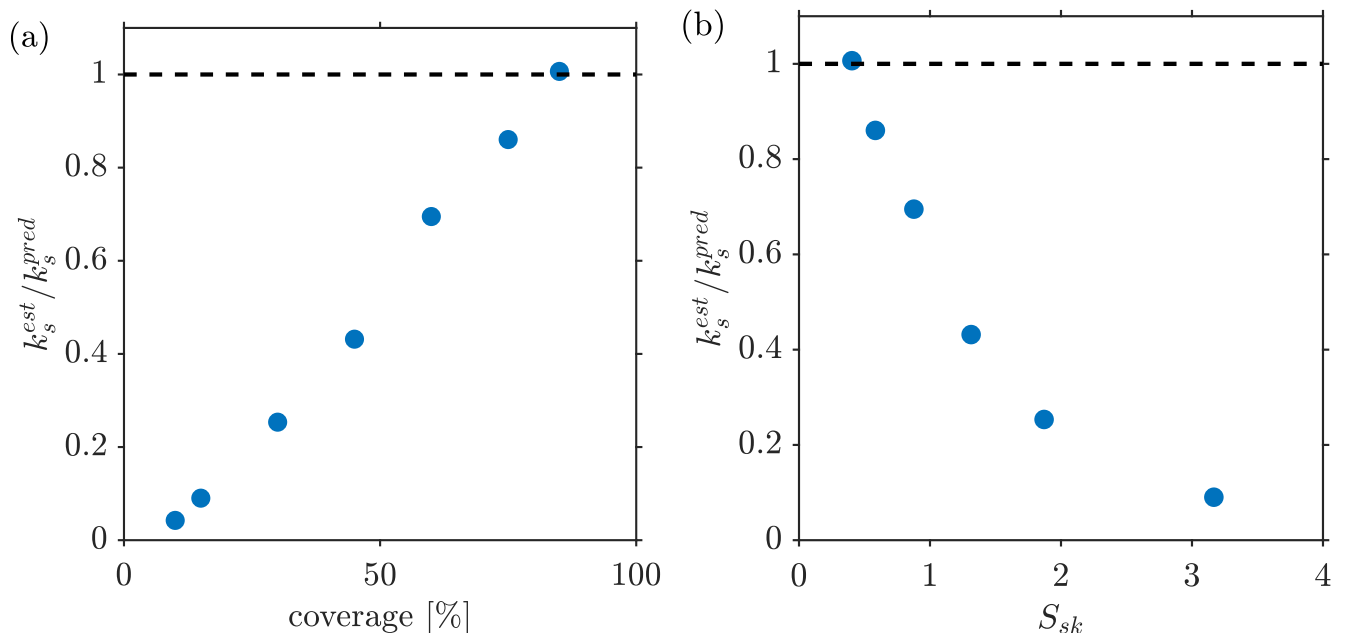


FIG. 5: Ratio of estimated to predicted equivalent sand grain roughness vs (a) coverage and (b) skewness. The black dashed line indicates the ratio for a perfect prediction.

performed experiments of turbulent channel flow over pyramid shaped roughness at several inclination angles and heights, altering the rough surfaces' effective slope while maintaining a constant positive skewness. Finally, Forooghi *et al.* [33] used artificially generated irregular rough surfaces with systematically varied parameters; from their data three different series with different skewness values (A00 series with  $S_{sk} \approx 0.2$ , B70 series with  $S_{sk} \approx -0.34$ , and C70 series with  $S_{sk} \approx 0.67$ ) are shown. For all the above data sets, a very similar trend is observed - an increase in the roughness function for low effective slope and an approximate saturation of the roughness effect for  $ES \gtrsim 0.35$ .

Comparing to the results from the barnacle covered surfaces, a similar increase is observed up to an effective slope value of  $ES \approx 0.4$  (corresponding to 60% coverage). However, as  $ES$  is increased further, a drop in  $\Delta U^+$  is observed, unlike the saturation that is seen for the other data sets. One factor that is likely to contribute to this deviation from the expected saturation with  $ES$  is that for the barnacle surface the skewness drops as  $ES$  increases. The cases with the highest effective slope have the lowest skewness, which is in line with the empirical relationship of Flack *et al.* [59] where a decrease in the roughness effect with decreasing (positive) skewness is predicted. For the data of Leonardi and Castro [26] a similar drop at high  $ES$  would be observed, since for cube roughness surface skewness also decreases with increasing planform and frontal solidity. However, surface skewness may not be the only contributing factor, as in the data of MacDonald *et al.* [52] also a drop in  $\Delta U^+$  is observed for high frontal solidity and high effective slope even though their sinusoidal egg-carton surfaces are all neutrally skewed.

Next to the frontal solidity/effective slope, skewness is probably the most widely investigated topographical roughness parameter. Flack *et al.* [59] developed the following empirical relationship for predicting the equivalent sand-grain roughness  $k_s$  based on the root mean square roughness height  $S_q$  and the surface skewness  $S_{sk}$ :

$$k_s^{pred} = aS_q(1 + S_{sk})^b \quad (2)$$

where the constants  $a$  and  $b$  depend on whether the surface is positively, neutrally, or negatively skewed. Since the present surfaces cover a wide range of skewness, it is of interest whether their roughness effect shows a similar skewness dependency as predicted by the empirical relationship (2). We estimated the approximate equivalent sand grain roughness of the surfaces based on  $\Delta U^+$  using the approach described in Chung *et al.* [46]

$$\frac{k_s^{est}}{S_q} = \frac{\exp(\kappa(\Delta U^+ - A + B_s(\infty)))}{S_q^+} \quad (3)$$

where  $\kappa \approx 0.4$  and  $A - B_s(\infty) \approx -3.5$ .

Figure 5 shows the ratio of the estimated equivalent sand grain roughness to the predicted equivalent sand grain roughness using  $a = 2.48$  and  $b = 2.24$  as fitted by Flack *et al.* [59] for positively skewed surfaces. For the highest

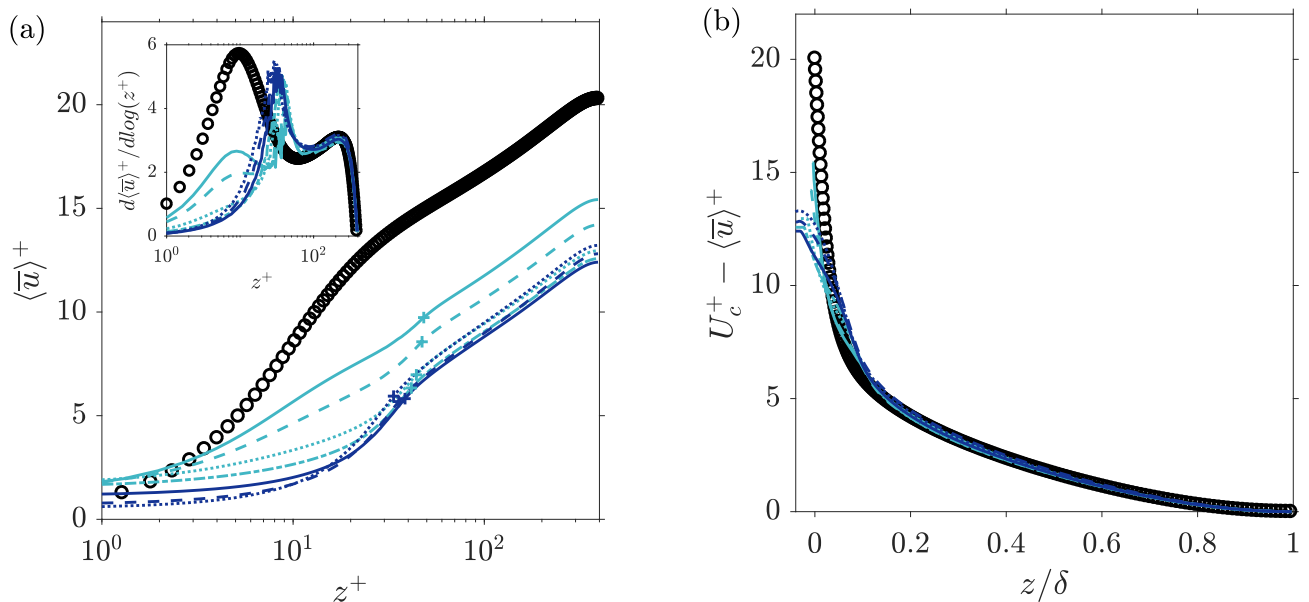


FIG. 6: (a) Mean streamwise velocity profiles of all coverage cases; the crosses indicate the maximum barnacle height, the inset plot shows the profile differentiated with respect to  $\log(z^+)$ ; (b) mean velocity defect profile. Line styles for the different coverage cases are given in Table II; black circles indicate smooth wall data.

213 coverage, the predicted and the estimated equivalent sand grain roughness agree well. However, this is not the case for  
 214 the lower coverages, where there is a significant over-prediction of the equivalent sand grain roughness which worsens  
 215 as the coverage decreases. Overall, the empirical relationship (2) appears to work well for moderate skewness values,  
 216 but fails to give a good prediction for the highly skewed surfaces. This can be attributed to the fact that this empirical  
 217 relationship was developed based on data for moderately skewed surfaces  $S_{sk} \lesssim 1$ .

218

## B. Mean velocity profile

219 The mean streamwise velocity profile, presented in figure 6 (a), clearly shows the increase and the subsequent  
 220 decrease in the roughness function beyond 60% coverage. All profiles show approximately logarithmic behaviour [51  
 221 and 60] above  $z^+ \approx 60$ , i.e., closely above the maximum barnacle height. The velocity defect profile (see figure 6  
 222 (b)) shows an excellent collapse of all profiles on the smooth-wall case above  $z/\delta \approx 0.15$  indicating that outer-layer  
 223 similarity is recovered in all cases.

224 In the near-wall region, clear differences can be observed between the roughness cases. Within the roughness layer,  
 225 the mean streamwise velocity decreases with increasing coverage (see figure 7 (a)). In the upper part of the roughness  
 226 layer, the 85% coverage case deviates from this trend and exhibits a more rapid increase in the mean streamwise  
 227 velocity than the 60% and 75% coverage cases resulting in the lower roughness function measured for this case. For  
 228 cases with low to moderate coverage, a relatively uniform rate of increase in the mean streamwise velocity profile can  
 229 be observed over the upper part of the roughness layer (see figure 7 (b)). In contrast, an inflection point emerges  
 230 for the cases with higher coverage. This inflection point falls between the maximum and minimum barnacle height  
 231 and becomes more pronounced as surface coverage increases. Inflection points have been observed for the streamwise  
 232 velocity profile for turbulent boundary layers over plant canopies [61] and in turbulent channel flow over regular sparse  
 233 canopies [62]. A similar feature can also emerge when roughness is modelled using the parametric forcing approach  
 234 [63, 64].

235 At high coverage the mean streamwise velocity deep within the rough surface decreases, with the appearance of  
 236 weak net reverse flow  $\langle \bar{u} \rangle < 0$  at 75% and 85% coverage within the lower part of the roughness layer leading to a  
 237 stronger retardation of the flow within the lower part of the roughness layer compared to the flow in its upper part.  
 238 Above the rough surface, the derivative of the mean velocity profile soon collapses on the values for the smooth wall  
 239 case, indicating that direct roughness effects impact the mean flow profile only in the immediate vicinity of the rough  
 240 surface.

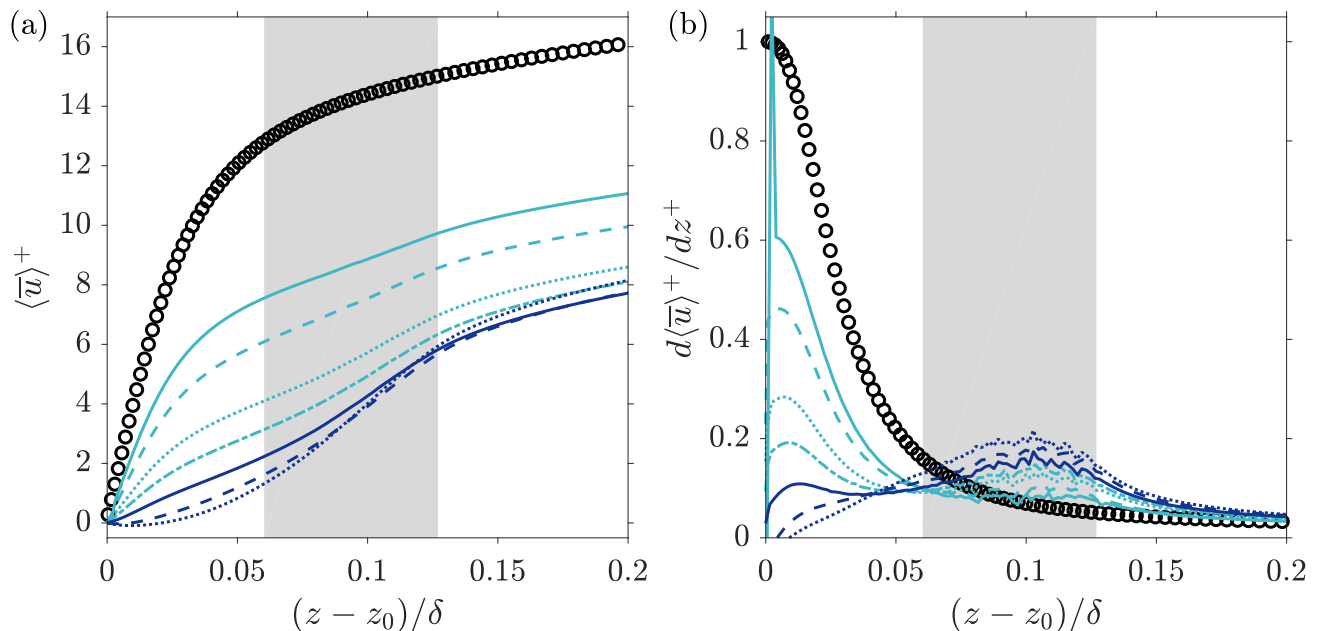


FIG. 7: (a) Mean streamwise velocity profiles close to the wall; (b) linear derivatives of the same profiles. Line styles for the different coverage cases are given in Table II; black circles indicate smooth wall data. The areas shaded in grey indicate the range of barnacle heights.

241

### C. Reynolds and dispersive stresses

242 The presence of roughness induces spatial inhomogeneities in the turbulent flow field near the wall, marking a region  
 243 termed the roughness sublayer [65]. To investigate the flow properties in this region, we apply the triple decomposition  
 244 of Raupach and Shaw [66]. For the  $u$ -component of the velocity field this gives

$$u(x, y, z, t) = \langle \bar{u} \rangle(z) + \tilde{u}(x, y, z) + u'(x, y, z, t), \quad (4)$$

245 where  $\langle \bar{u} \rangle(z)$  is the time and plane-averaged streamwise velocity component of the velocity field,  $\tilde{u}(x, y, z) = \bar{u}(x, y, z) -$   
 246  $\langle \bar{u} \rangle(z)$  is the spatial variation in the time-averaged streamwise velocity, and  $u'(x, y, z, t) = u(x, y, z, t) - \bar{u}(x, y, z)$   
 247 denotes the instantaneous fluctuation of  $u$  around the local time-averaged value of the velocity field. The decomposition  
 248 of the spanwise,  $v$ -, and wall-normal,  $w$ -, components of the velocity field is analogous. In the time- and plane-averaged  
 249 Navier-Stokes equations, the local turbulent fluctuations give rise to the Reynolds stresses  $\langle u'w' \rangle$ ,  $\langle u'v' \rangle$ , etc., while  
 250 the roughness-induced spatial variations in the time-averaged flow field induce the dispersive stresses  $\langle \tilde{u}\tilde{u} \rangle$ ,  $\langle \tilde{u}\tilde{w} \rangle$ , etc.

251 The Reynolds and dispersive stresses are shown in figures 8 to 11. The Reynolds stress profiles collapse in the  
 252 outer part of the flow onto the smooth-wall data, and no significant dependency on the degree of surface coverage is  
 253 observed (see inset panels in figures 8 (a) to 11 (a)). The following discussion therefore focusses on the behaviour of  
 254 the Reynolds and dispersive stress profiles within and in the near vicinity of the rough surface (see main panels in  
 255 figures 8 to 11).

256 Below the highest barnacle height, the streamwise normal Reynolds stress (see figure 8 (a)) shows for all coverages  
 257 a reduction in magnitude compared to the smooth wall reference case, decreasing with increasing coverage. This is  
 258 consistent with the decrease of the mean flow velocity within the rough surface with increasing coverage.

259 The peak streamwise Reynolds stress occurs around the maximum barnacle height for coverage of 15% or higher.  
 260 For the 10% coverage case two distinct peaks can be observed - a peak close to maximum barnacle height as for the  
 261 other cases, and an inner, slightly higher, peak located at  $\bar{z}^+ \approx 18$ , close to the wall-normal location for the peak  
 262 location for the streamwise Reynolds stress in the smooth channel reference case. While only a single peak can be  
 263 observed for the other surfaces, for the low coverage cases a sharp increase of the streamwise Reynolds stress can be  
 264 seen close to the location of the inner peak for the 10% case. This feature becomes less pronounced with increasing  
 265 coverage and fully disappears for the highest coverage cases (75% and 85%).

266 The 'outer' peak at approximately maximum barnacle height is decreasing for cases with 10% - 30% coverage; as  
 267 coverage is increased further this trend is reversed and an increase in the peak values is observed with the highest  
 268 peak value occurring for the 85% coverage case; the cases with the lowest peak values thus tend to yield the highest

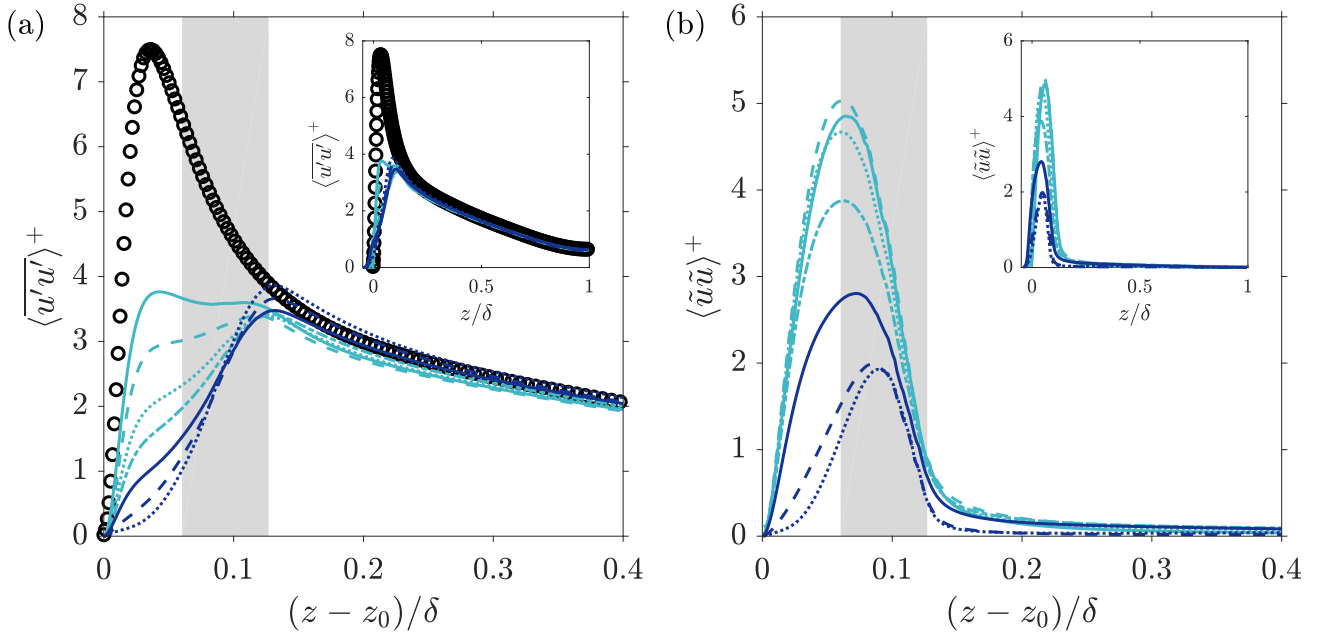


FIG. 8: Streamwise Reynolds (a) and dispersive stresses (b). The area shaded in grey indicates the range of barnacle heights. Line styles for the different coverage cases are given in Table II; black circles indicate smooth wall data. The areas shaded in grey indicates the range of barnacle heights.

269  $\Delta U^+$  values. A change in curvature of the profile in the near-wall region from negative, for the more sparsely covered  
 270 cases, to positive, for the densely covered ones, is visible. This leads to reduced streamwise velocity fluctuations in  
 271 the near wall region for increased solidity values. A damping of the rms velocity fluctuations with increasing frontal  
 272 solidity was also observed by MacDonald *et al.* [52], however, no double peak feature appears in their results. In the  
 273 study of Leonardi and Castro [26] on regular staggered cube roughness of varying planform (and frontal) solidity a  
 274 decrease in the streamwise Reynolds stress with increasing solidity within the roughness layer was observed; closely  
 275 above the roughness the highest solidity surface gave rise to the highest streamwise Reynolds stress values which is  
 276 consistent with the current observations.

277 Florens *et al.* [67] performed experiments of flow over roughness with cubical elements with a frontal solidity of 0.19,  
 278 which corresponds to a 19% coverage at  $Re_\tau = 460$ . The streamwise normal Reynolds stresses in their experiments  
 279 increase rapidly in the near-wall region, producing an inner peak, and a higher peak at the cubes' cusp. This behaviour  
 280 is very similar to the barnacle cases with 10% and 15% coverage.

281 The streamwise dispersive normal stress,  $\langle \tilde{u}\tilde{u} \rangle$ , corresponds to the spatial variance of the streamwise component  
 282 of the time-averaged velocity field. As expected, the highest levels of dispersive streamwise normal stress (see figure  
 283 8 (b)) occur below the maximum barnacle height. The maxima of the streamwise dispersive stresses exceed the  
 284 magnitude of the streamwise Reynolds stress values for the cases with low coverage, whereas for high coverage, the  
 285 streamwise dispersive stresses peaks are lower than their Reynolds stress equivalents. The highest peak is observed  
 286 for the case with 15% coverage and the peak for the 10% coverage case is slightly lower. In the other cases, the  
 287 maxima of the streamwise dispersive stress profiles show a descending behaviour with increasing coverage, with the  
 288 peak values of the two cases with highest coverage (75% and 85%) having almost identical magnitude. At the same  
 289 time, the peak location moves further away from the wall indicating that strong interaction between the mean flow  
 290 and rough surfaces now mainly occurs in the upper part of the rough surface.

291 The high peak values observed for low coverage cases are indicative of the dispersive stress definition which quantifies  
 292 the spatial inhomogeneity in the time-averaged flow produced by the presence of roughness. When more roughness  
 293 elements are placed on the flat surface, surface roughness becomes more homogeneous and fewer bald patches remain.  
 294 With low roughness homogeneity and greater sparsity, there is greater local divergence from the mean streamwise  
 295 velocity values, producing high dispersive stress values. Similar behaviour was observed by Leonardi and Castro [26]  
 296 who found a decrease in the peak value of streamwise dispersive stresses with increasing solidity for regular staggered  
 297 cube roughness, and Sharma and García-Mayoral [68] who observed a similar decrease in the streamwise dispersive  
 298 stresses for high frontal solidity for dense filament roughness.

299 The peak spanwise Reynolds stresses (see figure 9 (a)) occur around the height of the highest barnacle for the cases  
 300 with low coverage with a slightly elevated peak level compared to the smooth-wall case. With increasing coverage,

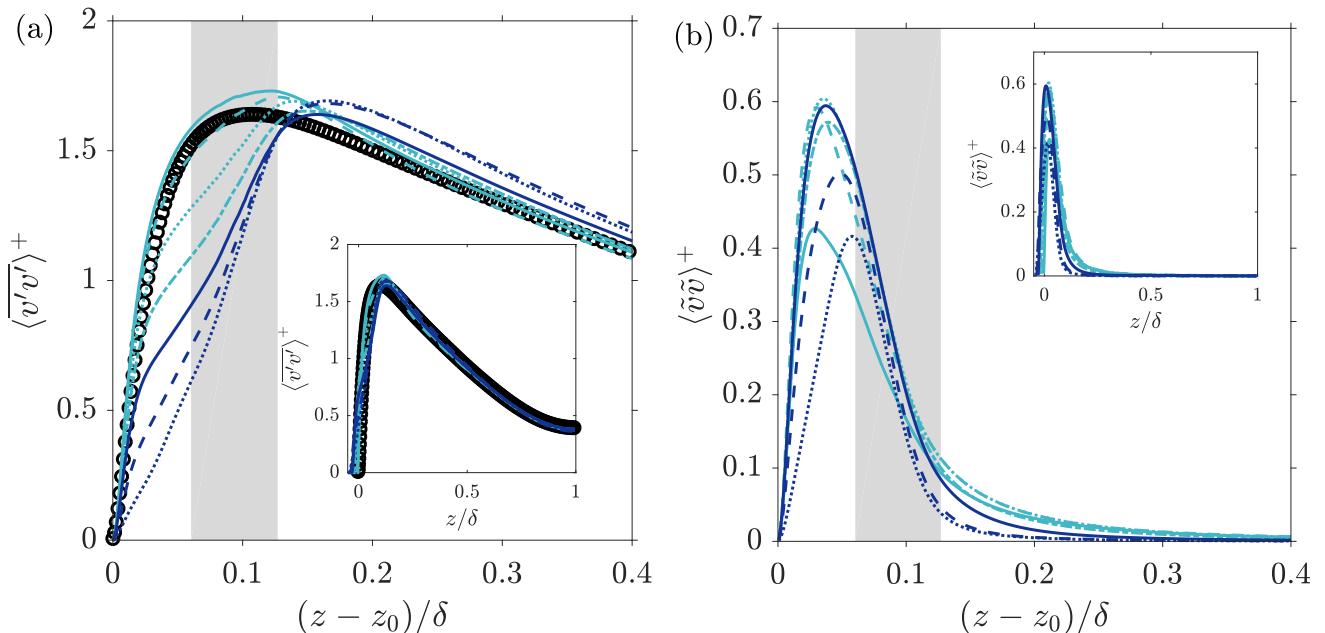


FIG. 9: Spanwise Reynolds (a) and dispersive stresses (b). The area shaded in grey indicates the range of barnacle heights. Line styles for the different coverage cases are given in Table II; black circles indicate smooth wall data. The areas shaded in grey indicates the range of barnacle heights.

301 the peak location moves above the rough surface and a reduction of spanwise velocity fluctuations can be observed  
 302 within the rough surface which is consistent with the decrease in the streamwise velocity fluctuations within the rough  
 303 surface. In contrast to the results for the streamwise velocity component, the levels of the spanwise dispersive stresses  
 304 are significantly lower, reaching peak values of less than 40% of the equivalent Reynolds stresses, which is comparable  
 305 to the levels observed for other forms of irregular roughness [69, 70]. As the coverage increases, the peak values first  
 306 increase before attaining approximately constant levels for the 15% to 60% cases before decreasing again. At the same  
 307 time, the peak location shifts further away from the surface as coverage is increased.

308 The spanwise dispersive stresses can be interpreted as a measure for the degree of in-plane circumnavigation of  
 309 roughness obstacles. For low solidity, large connected smooth patches remain for the current surfaces due to the  
 310 clustering inherent to the barnacle colonies. Therefore, there is relatively little need for circumnavigation of obstacles  
 311 and thus spanwise dispersive stress levels are lower. At the same time a barnacle cluster presents a sufficiently large  
 312 obstacle for the flow to move out of plane and above the barnacles (see also signature for wall-normal dispersive  
 313 stresses shown in figure 10(b)). On the other end of the solidity range, there is relatively weak streamwise flow within  
 314 the surface as the obstacles are densely spaced and local channeling of higher velocity fluid occurs. This entails in turn  
 315 relatively low levels of spanwise dispersive stress. The highest spanwise dispersive stress levels occur thus when there  
 316 are many roughness obstacles which are still sufficiently widely spaced to be exposed to a strong mean streamwise  
 317 velocity and which can induce locally significant spanwise motion to the mean flow, i.e., for the current surfaces at  
 318 the intermediate coverage values.

319 The behaviour of the wall-normal Reynolds stress (see figure 10 (a)) resembles that of the spanwise Reynolds stress.  
 320 In the roughness layer, the wall-normal Reynolds stress decreases with increasing coverage; however, compared to  
 321 the spanwise Reynolds stresses this reduction extends further into the flow. As a result, the peak wall-normal stress  
 322 occurs for all cases above the highest barnacle height and the peak location moves outwards as coverage increases.  
 323 The highest peak value can be observed for the 10% coverage case which exceeds the smooth-wall levels. The peak  
 324 values reduce with increasing coverage attaining an approximately constant value for 60% coverage and above. A  
 325 monotonous decrease of  $\langle w'w' \rangle$  with increasing solidity was also observed by Leonardi and Castro [26] for uniform cube  
 326 roughness and by MacDonald *et al.* [52] for egg-carton roughness, but in their simulations, the peaks occurred closely  
 327 above the roughness crests and no outwards movement of the peak location with increasing coverage was observed.  
 328 The differences in peak location trends can be attributed to the non-uniformity of the current surface where there is  
 329 no single crest location but a distribution of barnacle heights.

330 The levels attained by the wall-normal dispersive stresses (see figure 10 (b)) are also significantly lower than for  
 331 the corresponding Reynolds stresses, an observation that is consistent with results for other irregular rough surfaces  
 332 [69, 70]. It is noticeable that the peak values of the wall-normal stress and the levels sustained above the maximum

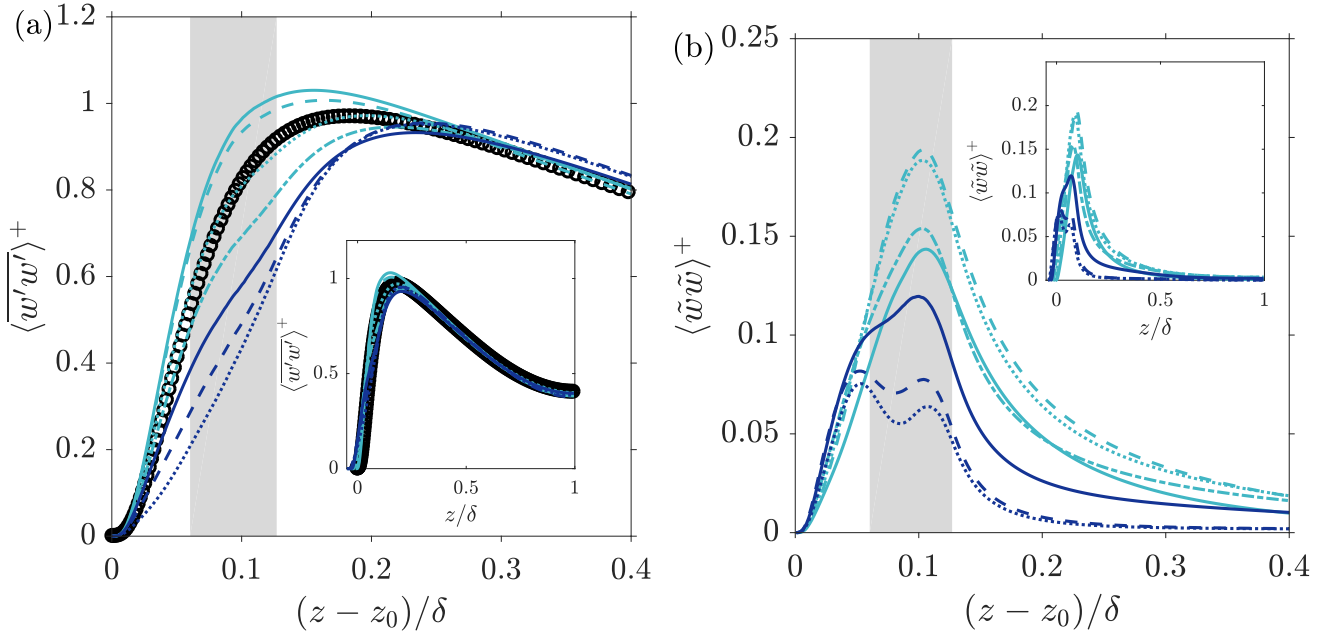


FIG. 10: Wall-normal Reynolds (a) and dispersive stresses (b). Line styles for the different coverage cases are given in Table II; black circles indicate smooth wall data. The areas shaded in grey indicates the range of barnacle heights.

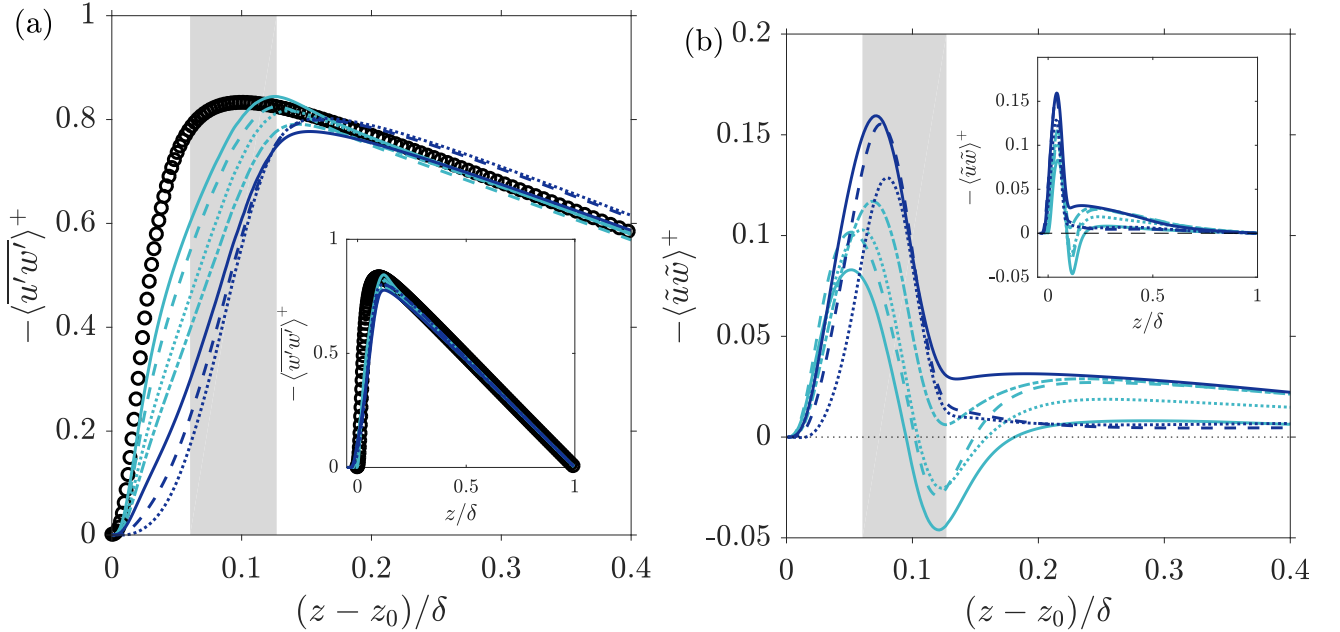


FIG. 11: Reynolds (a) and dispersive (b) shear stresses. Line styles for the different coverage cases are given in Table II; black circles indicate smooth wall data. The areas shaded in grey indicates the range of barnacle heights.

333 barnacle height are higher for the lower coverage surfaces, especially the 15% and 30% coverage cases. This can  
 334 be attributed to the fact that the low coverage surfaces have several distinct clusters of barnacles, and each cluster  
 335 effectively acts as a larger obstacle, encouraging the flow to move on larger, i.e. cluster-scales, over the obstacle. For  
 336 the high coverage cases, the clustered nature of the surface increasingly disappears due to merging of clusters, and  
 337 thus the levels of wall-normal dispersive stress decrease. However, a new feature emerges as coverage increases - a  
 338 second, inner peak deep within the roughness layer. This peak can be associated with increasing levels of recirculating  
 339 flow within the gaps the tightly-packed barnacles of the high coverage surfaces and be linked to the net reverse flow  
 340 observed in the mean streamwise velocity profile deep within the rough surface at high coverage.

341 The peak for the Reynolds shear stress (see figure 11 (a)) is located at a higher wall-normal location compared  
 342 to the smooth wall reference case in all cases. This is due to significant contributions of the dispersive shear stress  
 343 in the upper part of the roughness layer. The flow over the 10% coverage case develops the highest shear Reynolds  
 344 stress peak, located near the maximum barnacle height. As the surface coverage increases the Reynolds shear stress  
 345 peak decreases and moves further outward. The lowest peak is found at 60% coverage, while the 75% and 85%  
 346 cases exhibit slightly higher peak values. Within the roughness layer, a strong reduction of the Reynolds shear stress  
 347 compared to the smooth wall values can be observed. As the 75% and 85% coverage cases are the ones with reduced  
 348 roughness function values, compared to the maximum at 60%, it appears that a similar differentiation is only observed  
 349 over the maximum roughness height and not within the near-wall region, where a monotonous reduction is observed  
 350 with increasing solidity. The observed near-wall trend with increasing solidity agrees well with the observations by  
 351 MacDonald *et al.* [52] and Leonardi and Castro [26]. Further away from the wall, the Reynolds shear stress profiles  
 352 collapse with the smooth wall case, showing that the influence of roughness is restricted to the near-wall region (see  
 353 inset of figure 11 (a)).

354 The most complex behaviour of all stress profiles considered is exhibited by the dispersive shear stresses (see figure  
 355 11 (b)). Whilst the absolute levels of the dispersive shear stresses are low, they have a strong impact on the momentum  
 356 balance in the flow [71]. In all cases, a peak emerges within the roughness layer. The peak moves outwards with  
 357 increasing coverage; its magnitude increases up to a coverage of 60% and then starts to fall for the 75% and 85%  
 358 coverage cases; thus the peak value roughly correlates with the roughness function. The profiles for the 75% and 85%  
 359 cases resemble that of the peaks-only case in [71] and of the densely covered surfaces studied by Forooghi *et al.* [72].  
 360 For low coverage, a characteristic feature emerges in the form of a pronounced minimum located approximately at the  
 361 maximum barnacle height, leading to negative values of  $-\langle\tilde{u}\tilde{w}\rangle$  for the 10%, 15%, and 30% coverage cases. The depth  
 362 of this minimum decreases with increasing coverage, and no negative values for  $-\langle\tilde{u}\tilde{w}\rangle$  are observed for the higher  
 363 coverage cases. While, typically, positive values  $-\langle\tilde{u}\tilde{w}\rangle$  are reported for rough surfaces, negative values for  $-\langle\tilde{u}\tilde{w}\rangle$   
 364 have been previously observed in other rough-wall related studies, see e.g., for flow over superhydrophobic surfaces  
 365 with streamwise grooves [73] and for irregular rough surfaces with strong spanwise anisotropy [69].

366 Overall, the dispersive stresses show the presence of inhomogeneities in the time-averaged flow fields, which drop to  
 367 very low values for  $(z - z_0)/\delta \gtrsim 0.4$ . In the recent study by Womack *et al.* [47], secondary flows, which extended to a  
 368 distance of the order of the boundary layer thickness from the wall, were observed in turbulent boundary layers over  
 369 surfaces composed of uniformly sized truncated cones in uniform random arrangements. These took the form of high  
 370 and low momentum pathways, similar to those observed in the experimental study by Mejia-Alvarez and Christensen  
 371 [74] for turbulent boundary layers over a rough surface based on a scan of turbine roughness [75]. For the current  
 372 case, while there are clear spatial variations in the mean flow fields close to the surfaces, no strong secondary flow  
 373 structures have been detected that extend to the channel half-height. This may be due to the different roughness  
 374 configuration. A further possible cause for the absence of strong large-scale secondary flow structures may be the  
 375 different type of flow configuration: In the present study, turbulent channel flow with roughness on both walls of the  
 376 channel and periodic boundary conditions in the streamwise and spanwise direction was simulated whereas the  
 377 referenced experimental studies used a turbulent boundary layer configuration. This is would be supported by the  
 378 observation made by Womack *et al.* [47] that in their boundary layer experiments the secondary flows were initiated at  
 379 the leading edge of the rough surfaces. Per its nature, this initiation mechanism is not possible for turbulent channel  
 380 flow with periodic boundary conditions, since there is no leading roughness edge. In the following, we therefore  
 381 focus on the characterisation of the mean flow within the rough surfaces and in their immediate vicinity where clear  
 382 structures emerge.

#### 383 D. Analysis of the time averaged flow field within roughness

384 The results for the dispersive and Reynolds stress profiles indicate that the flow within the rough surface shows  
 385 a very strong dependence on the level of coverage. In this section, the time-averaged flow within the rough surface  
 386 will be analysed in more detail using probability density functions (pdfs) and flow visualisations of the time-averaged  
 387 streamwise velocity field  $\bar{u}(x, y, z)$  (see figures 12, 13, and 14).

388 Pdfs of  $\bar{u}$  were sampled at four different wall-normal locations, corresponding  $0.1S_{z,max}$ ,  $0.3S_{z,max}$ ,  $0.5S_{z,max}$ , and  
 389  $0.8S_{z,max}$  above the smooth wall plane (see figure 12 (a) to (d)). Deep within the roughness layer (see figure 12 (a)  
 390 and (b)) there is a high probability for high  $\bar{u}$  values at low coverage (10% and 15%), due to the existence of large  
 391 smooth surface sections over which the flow is free to accelerate in the absence of obstacles (see figure 13 (a) and (b)).  
 392 A weak secondary peak is present at  $\bar{u} \approx 0$  which can be related to the small velocities in the wake and immediately  
 393 upstream of the barnacles.

394 For intermediate coverage (30%, 45%, and 60%), the flow deep within the rough surface becomes increasingly  
 395 obstructed as the barnacle clusters merge; the pdfs appear quite broad since there is a wide distribution of values for

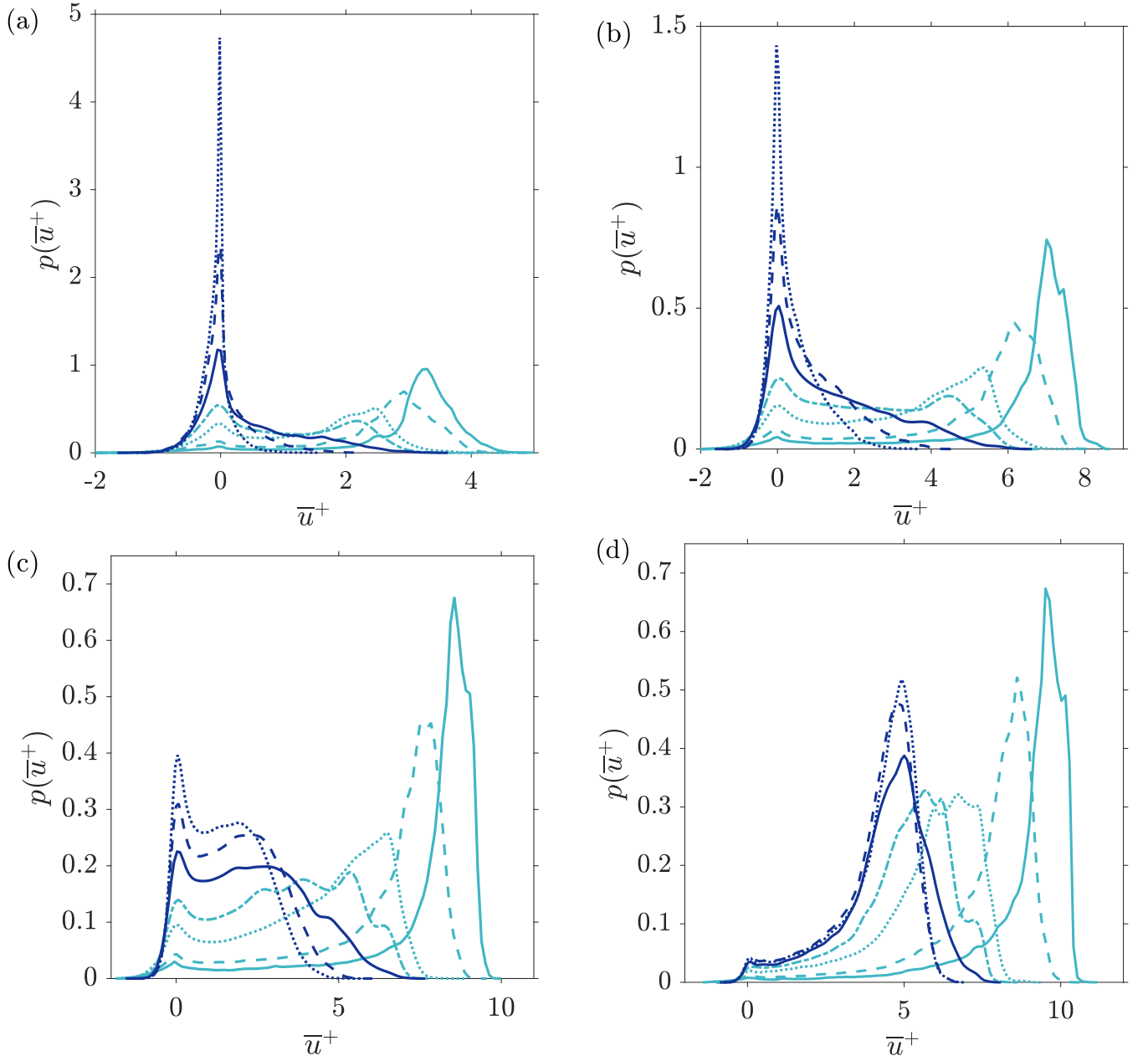


FIG. 12: Comparison of pdfs of the time averaged streamwise velocity component at wall-normal locations (a)  $0.1S_{z,max}$ , (b)  $0.3S_{z,max}$ , (c)  $0.5S_{z,max}$ , and (d)  $0.8S_{z,max}$  above the smooth settling plane. Line styles for the different coverage cases are given in Table II.

<sup>396</sup>  $\bar{u}$ . The remaining blank surface patches favour high velocities and, at the same time, the importance of low velocity  
<sup>397</sup> areas increases due to the higher number of barnacles which entails increased probability of low  $\bar{u}$  values in their  
<sup>398</sup> wakes and in the small gaps between closely spaced barnacles (see figure 13 (c) to (e)).

<sup>399</sup> In contrast, at high coverage (75%, and 85%) the pdfs of  $\bar{u}$  start to approach the shape of a  $\delta$ -function centred at  
<sup>400</sup>  $\bar{u} = 0$  indicating that the flow deep within the rough surface is largely stagnant. For the 75% coverage case a right  
<sup>401</sup> hand tail can be seen, indicating some localized higher mean flow velocities which are a consequence of channeling-like  
<sup>402</sup> behaviour (see figure 13 (f)). For the highest coverage of 85%, most of these channels are obstructed by the added  
<sup>403</sup> barnacles and only weak traces of channeling remain visible (see figure 13 (g)).

<sup>404</sup> With increasing distance from the smooth wall plane, i.e., at higher wall-normal locations, the mean of  $\bar{u}$  in all  
<sup>405</sup> cases is shifted to higher values and the pdfs of  $\bar{u}$  change their shape depending on the level of surface coverage. For  
<sup>406</sup> the low-coverage cases (10% and 15%), the pdfs retain approximately the same strongly negatively skewed shape at

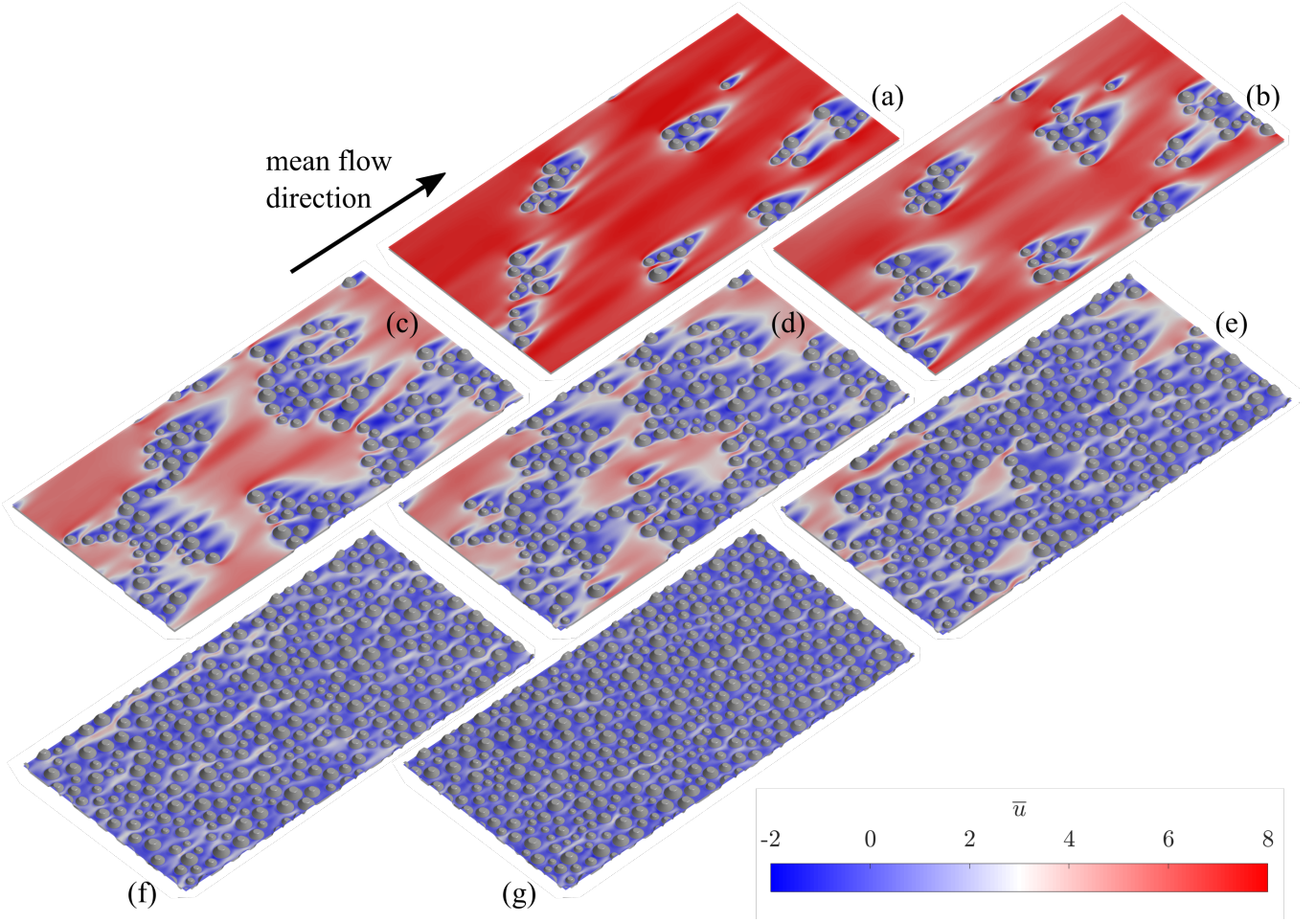


FIG. 13: Time-averaged streamwise velocity field  $\bar{u}^+(x, y, z)$  at  $0.3S_{z,max}$  above the smooth settling plane. (a) 10%, (b) 15%, (c) 30%, (d) 45%, (e) 60%, (f) 75% and (g) 85% coverage.

all wall-normal locations below the maximum roughness height. The appearance of the flow (see figure 14 (a) and (b)) remains qualitatively similar to the flow deep within the rough surface (see figure 13 (a) and (b)); the only significant change is that fewer wake regions remain visible at the higher locations, since the smaller barnacles are submerged.

For intermediate coverage (30%, 45%, and 60%), a broad flat distribution remains visible for  $0.3S_{z,max}$  and  $0.5S_{z,max}$  (see figure 12 (b) and (c)), but towards the upper end of the roughness layer the pdfs start to increasingly resemble the strongly negatively skewed shape of the pdfs for the lower coverage surfaces (see 12 (d)). This is because towards the upper end of the roughness layer the appearance of the flow is changed (see figure 14 (c) to (e)), since only the highest barnacles are exposed to the flow, the remaining low velocity areas are closely related to the wakes of the tall exposed barnacles, and large unobstructed areas emerge over which the flow can attain higher  $\bar{u}$  values. This explains the change of the pdfs to a more negatively skewed shape.

For the high coverage cases (75% and 85%) the pdfs undergo the strongest change in shape: for  $0.3S_{z,max}$  (see figure 12 (b)) the pdfs are strongly positively skewed, and there is still a single dominant peak at  $\bar{u} = 0$  which can be associated with nearly stagnant regions of the flow in areas of closely packed barnacles. At 50% of the maximum barnacle height (see figure 12 (c)) a second peak at  $\bar{u} \gg 0$  can be observed, but the pdfs remain positively skewed. Close to the top of the barnacles (see figure 12 (d)) the peak at  $\bar{u} \gg 0$  becomes dominant, the peak at  $\bar{u} = 0$  starts to disappear, and the pdfs now have a strongly negatively skewed shape. Since only the highest barnacles remain exposed at  $0.8S_{z,max}$ , most are sufficiently distanced from each other to allow the formation of small, individual wakes. The rest of the flow appears relatively uniform; some elongated areas of higher-speed velocity areas can be discerned which can be directly related to the channels of high speed fluid deeper within the rough surface. These observations explain the strong change in shape in the pdfs for  $\bar{u}$  when comparing the pdfs for the  $0.3S_{z,max}$  and  $0.8S_{z,max}$  locations.

Consequently, the flow behaviour can be classified into three categories according to surface coverage: The first category includes surfaces with low barnacle coverage (10% and 15%), where the barnacles form distinct clusters

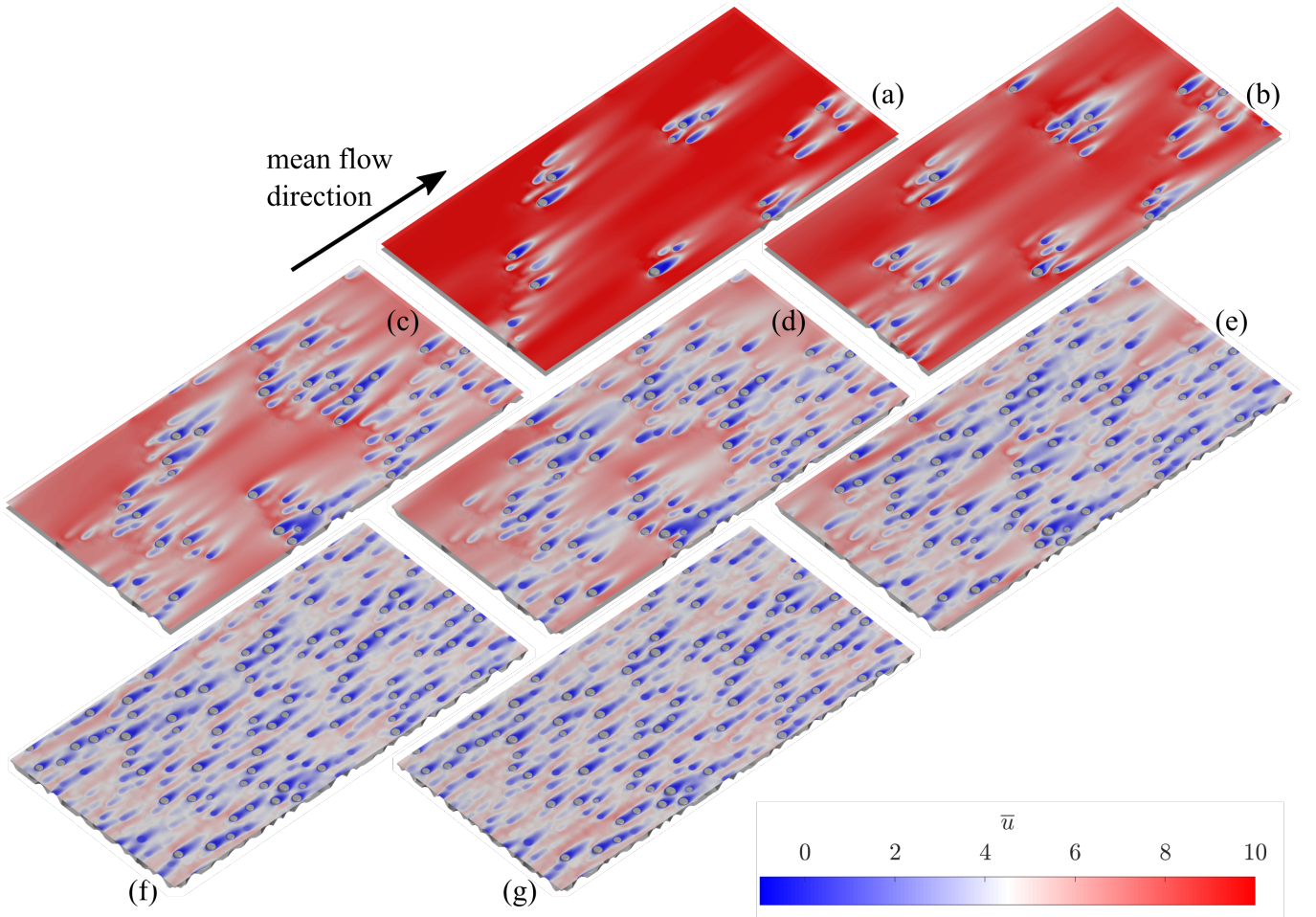


FIG. 14: Time-averaged streamwise velocity field  $\bar{u}^+(x, y, z)$  at  $0.8S_{z,max}$  above the smooth settling plane. (a) 10%, (b) 15%, (c) 30%, (d) 45%, (e) 60%, (f) 75% and (g) 85% coverage.

429 surrounded by large connected areas of smooth surface. In this case, the fluid flows around and above the barnacle  
 430 clusters, forming connected wake regions. Over the large interconnected smooth surface regions the velocity increases  
 431 and starts to return to a smooth wall-behaviour until the next barnacle cluster is encountered. The second category  
 432 includes surfaces with medium to high barnacle coverage (30%, 45%, and 60%), where barnacle colonies merge but  
 433 some smooth surface patches remain. In this case, the fluid experiences much stronger obstruction within the rough  
 434 surface and can only weakly accelerate over the remaining smooth surface patches that have not yet been colonised by  
 435 barnacles, with the rest of the flow field within the roughness sub-layer being characterized by barnacle wake regions  
 436 and nearly stagnant velocity regions between closely packed barnacles. The third category contains the heavily covered  
 437 surfaces (75% and 85% surface coverage), where the barnacles form a single continuous cluster with no large smooth  
 438 surface patches and only small gaps between barnacles. The flow field in this case appears as a continuous wake field  
 439 at low wall-normal locations, with the wake of a barnacle being connected to the stagnation areas of the downstream  
 440 adjacent ones. However, due to the tapered shape of barnacles and their random placement on the smooth surface,  
 441 irregular streamwise streaks of higher mean velocity can be observed which are the result of a channeling effect. Some  
 442 traces of this channeling effect remain visible at higher wall-normal locations. The overall behaviour of the densely  
 443 and sparsely covered surfaces resembles the categorization of flow over urban canopy roughness into isolated roughness  
 444 flow, wake interference flow, and skimming flow, as described by Oke [76].

445

### E. Imprint of the rough surface on the flow

446 For high coverage cases, deep within the rough surface, a large fraction of the fluid occupied area is filled with nearly  
 447 stagnant or recirculating flow. The mean streamwise velocity profile in the immediate vicinity of the wall shows for

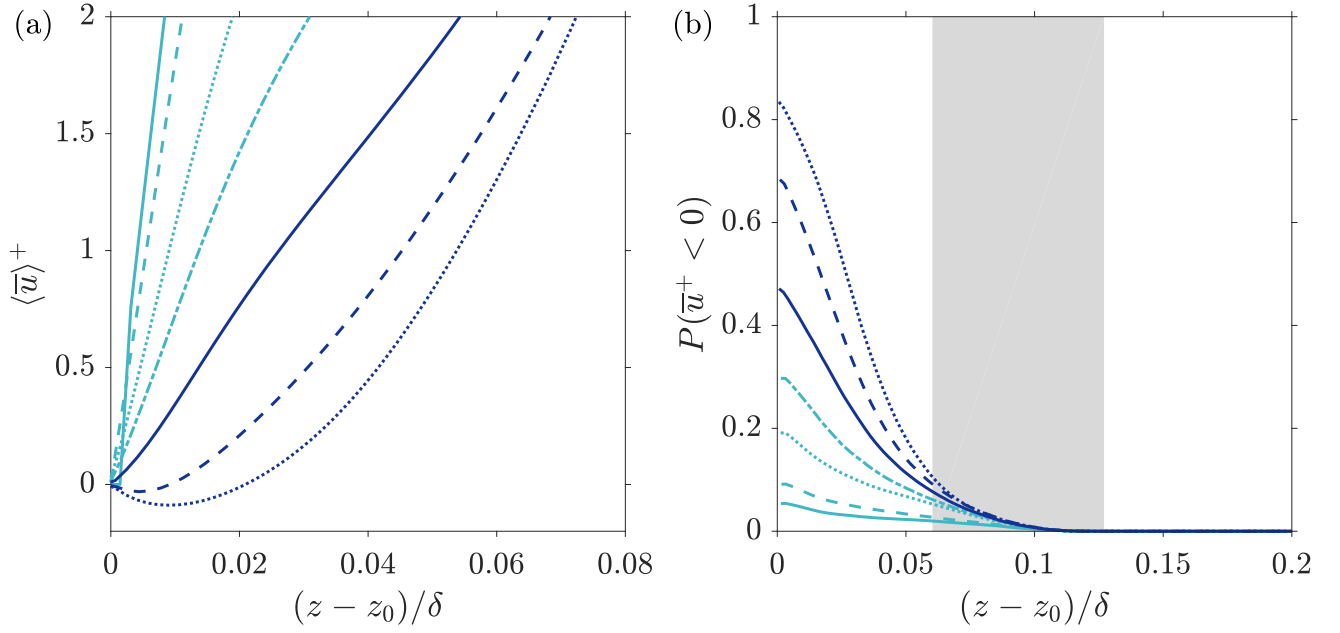


FIG. 15: (a) Mean streamwise velocity profiles within the roughness layer; (b) probability of reverse flow ( $\bar{u} < 0$ ) versus wall-normal location. Line styles for the different coverage cases are given in Table II.

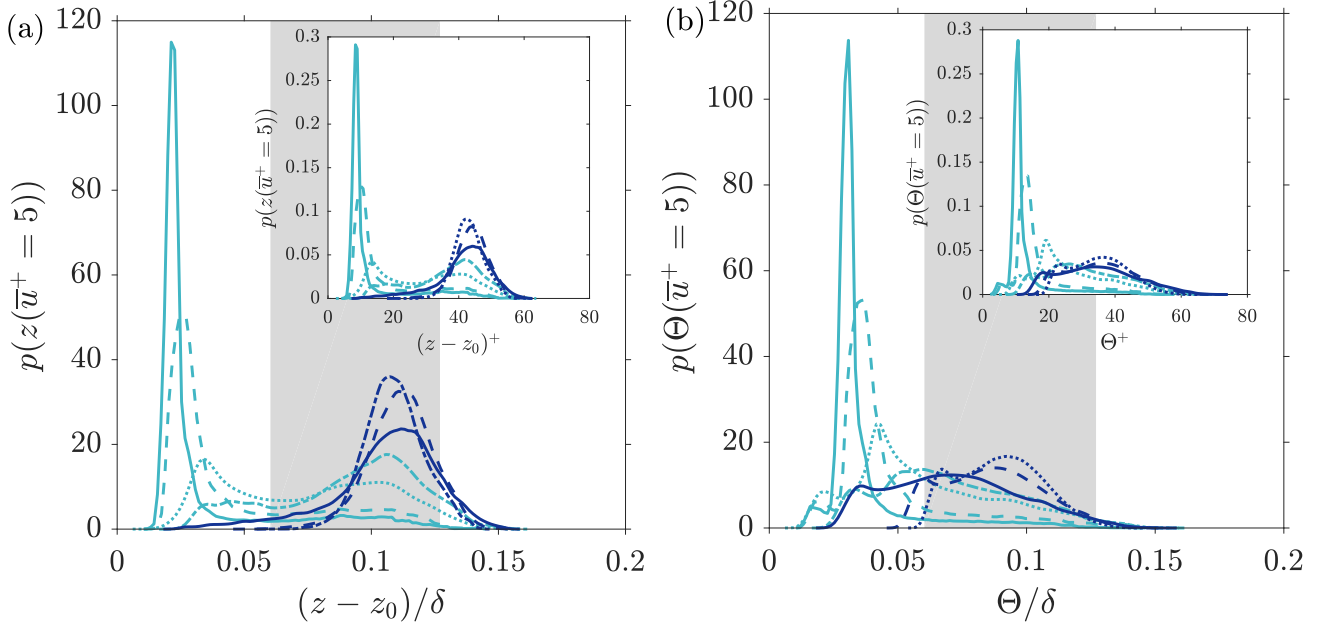


FIG. 16: (a) Pdf of the blanketing layer height; (b) pdf of the blanketing layer thickness  $\Theta$ . Line styles for the different coverage cases are given in Table II.

448 the 75% and 85% coverage cases a negative mean (see figure 15 (a)) indicating the predominance of weak reversed  
 449 flow. This observation is also supported by the probability of reversed flow  $\bar{u} < 0$  (see figure 15 (b)) which reaches  
 450 values above 0.5 for the 75% and 85% coverage cases as  $z_0$  is approached.

451 Reverse flow areas can have a ‘cushioning’ effect on the flow past a rough surface, since flow tends to skim above areas  
 452 of recirculating flow [51, 71]. For the present surfaces, reverse flow mainly forms in narrow gaps between roughness  
 453 features and in the near wake of the barnacles. One of the consequences of cushioning is that the flow passing the  
 454 rough surface effectively interacts only with a reduced frontal area of the roughness elements. The way the ‘bulk’ flow,  
 455 i.e., the time-averaged flow above the rough surface, experiences the roughness can be quantified using the concept of

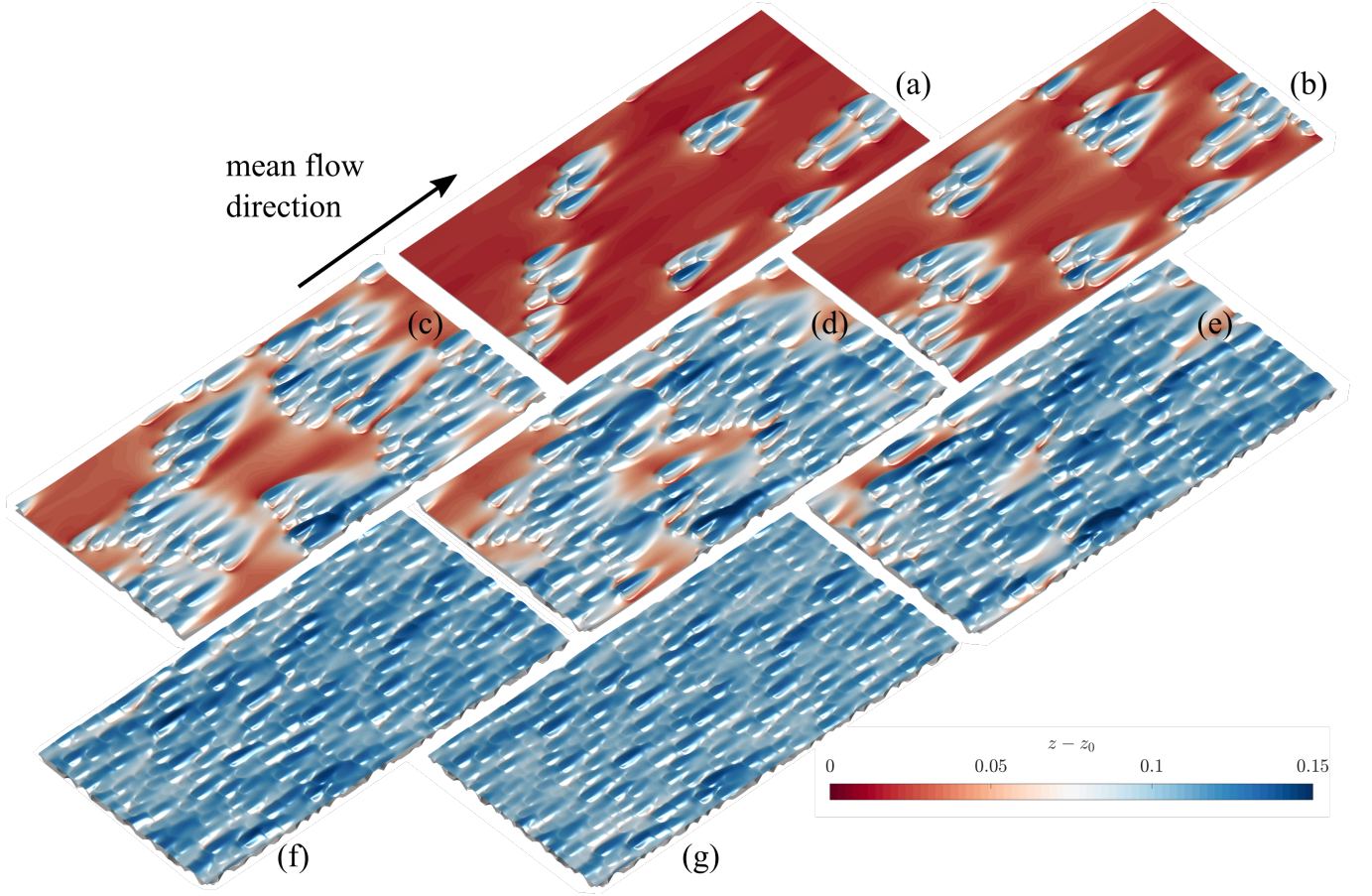


FIG. 17: Three dimensional representation of the blanketing layer for the surfaces with (a) 10%, (b) 15%, (c) 30%, (d) 45%, (e) 60%, (f) 75%, and (g) 85% barnacle coverage.

TABLE V: Topographical parameters of the blanketing layer  $B(x, y)$ , which is implicitly defined by the isosurface  $\bar{u}^+(x, y, z) = 5$ .  $\lambda_f^B$ : frontal solidity;  $ES^B$ : effective slope,  $S_a^B$ : mean roughness height;  $S_q^B$ : rms roughness height;  $S_{sk}^B$ : Skewness;  $S_{ku}^B$ : Kurtosis;  $L_{corr,x}^B$ : streamwise correlation length;  $L_{corr,y}^B$ : spanwise correlation length;  $\langle B \rangle - z_0$ : mean height above smooth wall;  $\min(B) - z_0$  minimum height of the blanketing layer above the smooth surface;  $c_{h,B}$ : cross correlation coefficient between  $h(x, y)$  and  $B(x, y)$

Coverage	$\lambda_f^B$	$ES^B$	$S_a^B/\delta$	$S_q^B/\delta$	$S_{sk}^B$	$S_{ku}^B$	$L_{corr,x}^B/\delta$	$L_{corr,y}^B/\delta$	$(\langle B \rangle - z_0)/\delta$	$(\min(B) - z_0)/\delta$	$c_{h,B}$
10 %	0.022	0.044	0.030	0.040	1.99	5.74	2.09	0.70	0.035	0.012	0.623
15 %	0.031	0.061	0.039	0.049	1.22	3.12	1.37	1.57	0.046	0.013	0.576
30 %	0.041	0.081	0.059	0.067	0.08	1.76	1.90	1.40	0.074	0.017	0.492
45 %	0.043	0.085	0.069	0.075	-0.48	2.38	2.14	1.28	0.091	0.023	0.420
60 %	0.042	0.085	0.076	0.079	-1.00	4.31	2.88	1.57	0.105	0.022	0.317
75 %	0.038	0.077	0.075	0.076	-0.33	3.50	2.71	0.36	0.111	0.049	0.236
85 %	0.035	0.069	0.067	0.068	0.075	3.02	2.69	0.14	0.109	0.057	0.255

the ‘blanketing layer’ [51]. The blanketing layer is defined as the iso-surface corresponding to  $\bar{u}^+(x, y, z) = 5$ . This singly-connected surface will be referred to by  $B(x, y)$  in the following; it should be noted that there is in general no explicit functional expression for  $B(x, y)$ , i.e., the surface  $B$  is in general only implicitly defined.

For a smooth-wall flow, the blanketing layer is a flat plane that is offset by  $z^+ = 5$  from the wall and corresponds to the upper end of the viscous sub-layer, i.e.,  $B(x, y) = 5\delta_\nu$  where  $\delta_\nu$  is the viscous length scale of the flow. For rough-wall flows, the concept of the viscous sub-layer ceases to exist, and the blanketing layer is strongly shaped by the underlying topography of roughness (see figure 17). However, due to processes such as wake formation behind surface peaks and the separation of the mean flow over surface indentations and narrow gaps, the blanketing layer

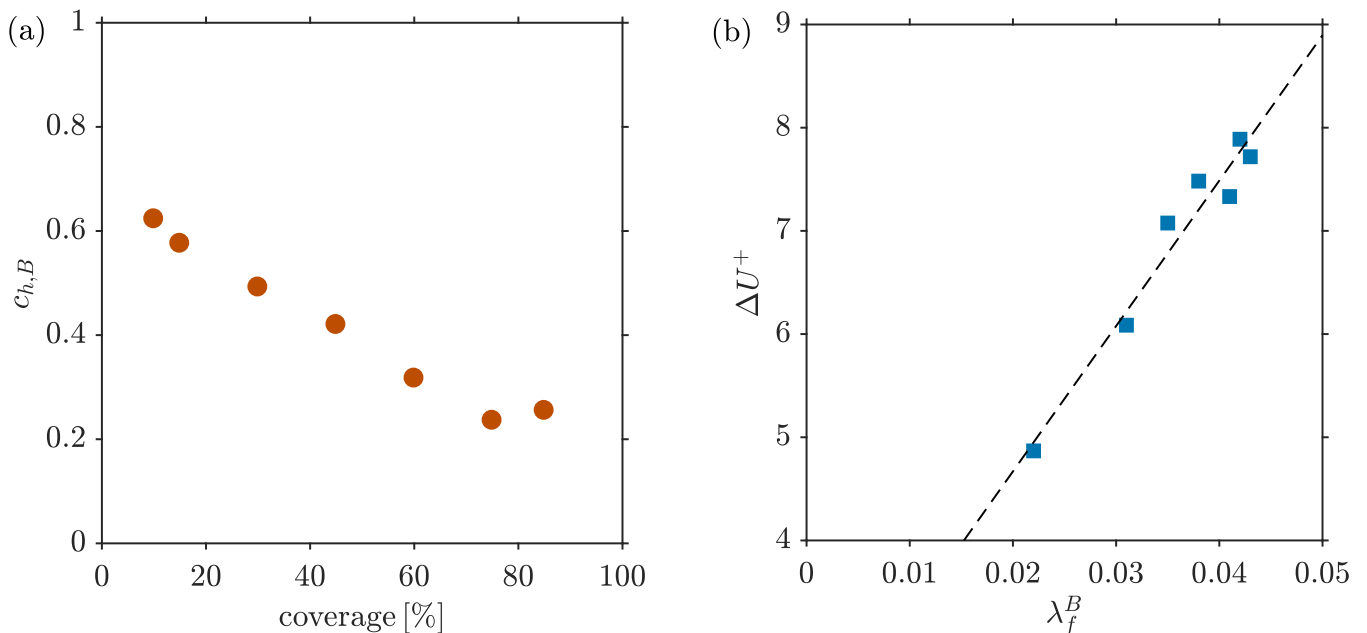


FIG. 18: (a) Cross-correlation coefficient  $c_{h,B}$  as a function of coverage; (b)  $\Delta U^+$  as a function of the frontal solidity of the blanketing layer. The fitted line corresponds to  $f(\lambda_f^B) = 140.9\lambda_f^B + 1.851$

cannot follow the topography of a rough surface perfectly, resulting a distribution of values for the blanketing layer thickness  $\Theta = B(x, y) - h(x, y)$  (see figure 16 (b)). The blanketing layer thickness for a smooth surface corresponds to a  $\delta$ -function with its peak at  $\Theta = 5\delta_\nu$ . It can be observed that for the low coverage cases, some traces of this peak remain visible at low thicknesses which can be associated with the relatively undisturbed flow over the large smooth-wall sections for these surfaces. A right hand tail to higher thicknesses can be observed as a result of the blanketing layer being further displaced relative to the rough surface in the near wake of the barnacles. For high coverage, there is a broad distribution of values for  $\Theta$  as a consequence of increasing cushioning of the flow.

Whilst the blanketing layer is a fluid dynamic property characterising changes in the mean flow induced by the underlying roughness, we can apply approaches from rough surface metrology to characterise its topography. The shape of the blanketing layer has been quantified for each case by computing its topographical parameters in analogy to the topographical parameters for rough surfaces (see Table V). It is immediately apparent by comparing figure 17 with figure 2, that with increasing coverage the blanketing layer conforms less to the underlying rough surface. This decreasing correlation between height map and blanketing layer can be quantified using the cross-correlation coefficient between the blanketing layer and the roughness height map which is defined as

$$c_{h,B} = \frac{\langle (B(x, y) - \langle B \rangle) (h(x, y) - \langle h \rangle) \rangle}{(\text{var}(B(x, y)) \text{var}(h(x, y)))^{1/2}} \quad (5)$$

where  $\text{var}$  indicates the variance. Since the flow separates in the wake of the barnacles, there is no perfect correlation between blanketing layer and height map even for the lowest coverage, but the computed value of 0.623 for  $c_{h,B}$  indicates a significant correlation between the height map and the blanketing layer at 10% coverage (see table V). As the coverage increases, from 10% to 75%,  $c_{h,B}$  decreases. A slight increase can be observed for the highest coverage (85%) compared to the 75% case (see figure 18 (b)). Due to the irregular nature of the rough surfaces, the slightly higher value of the 85% case cannot be related to any specific feature of this surface. For very high coverage, the cross-correlation may show an increasing trend due to the increased solidity of the surfaces. For example, for a roughness composed of uniform cubes, a cross-correlation coefficient of 1 should be approached in the limit of 100% coverage, where all the cubes merge to form a new flat solid surface. Since the current roughness elements are non-uniform in height and tapering, this limit will not be attained but the effect may be sufficient to cause the observed increase in the cross-correlation coefficient.

For low to medium coverage, the blanketing layer mean height moves further away from the smooth reference surface but it attains an approximately constant value for 60% coverage and above. The spatial structure of the blanketing layer also changes with increasing coverage: For moderate coverage (15% and 30%), it is nearly isotropic, i.e., the streamwise and spanwise correlation length are of similar magnitude. As coverage is increased further,

the blanketing layer starts to be dominated by elongated structures which can be related to the wake-interference phenomenon discussed above, where the distinct character of the wakes of individual barnacle roughness elements gets lost due to merging of wakes. The kurtosis value of the blanketing layer  $S_{ku}^B$  drops with increasing skewness from a moderately high value to a Gaussian value of approximately 3 - comparing these values to the corresponding topographical parameters for the underlying rough surfaces it is apparent that both the extremely high and low kurtosis values are attenuated by the cushioning effect. The skewness values are also influenced by the cushioning - in all cases, the  $S_{sk}^B < S_{sk}$ , i.e., due to the wake formation the barnacle roughness elements appear as less pronounced peaks to the outer flow. For medium to high coverage, the blanketing layer surface ceases to be peak-dominated and it exhibits negative skewness values due to the emerging streamwise narrow valleys that can be associated with the channelling effect. As the channeling effect starts to weaken at the highest coverage, the skewness of the blanketing layer approaches zero, i.e., the blanketing layer starts to resemble a Gaussian surface.

Finally, the frontal solidity and effective slope of the blanketing layer give rise to an interesting observation: with increasing coverage the frontal solidity / effective slope of  $B(x, y)$  firstly rises, reaching its maximum at 45% and 60% and then decreases at 75% and 85% coverage. The blanketing layer thus gives direct insight into the question why  $\Delta U^+$  decreases for high frontal solidity; this happens because the solidity of the surface perceived by the bulk flow (here quantified using the blanketing layer) starts to decrease (see figure 18 (b)).

#### IV. CONCLUSIONS

The fluid dynamic behaviour of barnacle-type rough surfaces with increasing coverage was investigated using direct numerical simulations of turbulent channel flow at  $Re_\tau = 395$ . Whilst the present surfaces were inspired by a typical form of marine biofouling, barnacle-type roughness can also serve as a general example for irregular roughness composed of roughness elements of randomised height and shape. Unlike the more homogeneous regular and irregular rough surfaces considered in most previous investigations of the fundamental properties of rough-wall turbulence, the current barnacle-type rough surfaces are characterised by clustering of roughness features at low plan-form solidity. This leads to some distinct behaviour at low coverage, as traces of smooth wall behaviour are recovered over the large connected smooth section that are characteristic of these surfaces. Analogies between the present surfaces and other forms of roughness can be made to urban flows, as the observed mean flow behaviour essentially follows the categorisation of Oke [76].

The roughness function followed the expected trend with frontal solidity but did not exhibit the expected saturation of the roughness effect with high effective slope. The decrease at high effective slope reinforces that other topographical parameters, such as skewness, also have a strong influence on the roughness effect (see discussion in [46]). However, when considering the ‘perceived’ roughness from the perspective of the flow that passes over roughness, here quantified using the blanketing layer, a simpler behaviour emerges, namely a linear increase in the roughness function with increasing effective slope of the blanketing layer. It remains to be established whether this would also apply for other forms of roughness. If a reliable mapping between rough surface and blanketing layer topography could be achieved, simpler relationships between topographical parameters and the roughness effect may emerge. However, due to the complex nature of separation and reattachment over a rough surface, the emergence of channeling within the roughness, as well as the wide range of roughness topographies encountered in engineering and geophysical applications, a general mapping may be difficult to achieve.

#### ACKNOWLEDGEMENTS

We gratefully acknowledge support by the United Kingdom Engineering and Physical Sciences Research Council (EPSRC) under grant number EP/P009875/1 and access to the United Kingdom’s National HPC facility ARCHER hosted by EPCC Edinburgh.

- 
- [1] J A Lewis, “Marine biofouling and its prevention on underwater surfaces,” *Materials Forum* **22**, 41–61 (1998).
  - [2] Woods Hole Oceanographic Institution, *Marine biofouling and its prevention* (U.S. Naval Institute, Annapolis, Maryland, 1952) prepared for Bureau of Ships, Navy Department.
  - [3] S. M. Evans, A. C. Birchenough, and M. S. Brancato, “The TBT ban: Out of the frying pan into the fire?” *Marine Pollution Bulletin* **40**, 204–211 (2000).
  - [4] L. Gipperth, “The legal design of the international and European Union ban on tributyltin antifouling paint: Direct and indirect effects,” *Journal of Environmental Management* **90**, S86–S95 (2009).

- 542 [5] M Salta, L Chambers, J Wharton, R Wood, J F Briand, Y Blache, and K R Stokes, “Marine fouling organisms and their  
543 use in antifouling bioassays,” in *European Corrosion Congress (EUROCORR)* (2009).
- 544 [6] M. P. Schultz and G. W. Swain, “The influence of biofilms on skin friction drag,” *Biofouling* **15**, 129–139 (2000).
- 545 [7] M. P. Schultz, “Turbulent boundary layers on surfaces covered with filamentous algae,” *Journal of Fluids Engineering* **122**,  
546 357–363 (2000).
- 547 [8] M. P. Schultz, “Frictional resistance of antifouling coating systems,” *Journal of Fluids Engineering* **126**, 1039–1047 (2004).
- 548 [9] J. Barros, E. Murphy, and M. P. Schultz, “Particle image velocimetry measurements of the flow over barnacles in a  
549 turbulent boundary layer,” in *18th International Symposium of the Application of Laser and Imaging Techniques to Fluid  
550 Mechanics* (2016).
- 551 [10] J. P. Monty, E. Dogan, R. Hanson, A. J. Scardino, B. Ganapathisubramani, and N. Hutchins, “An assessment of the ship  
552 drag penalty arising from light calcareous tubeworm fouling,” *Biofouling* **32**, 451–464 (2016).
- 553 [11] K. M. Berntsson and P. R. Jonsson, “Temporal and spatial patterns in recruitment and succession of a temperate marine  
554 fouling assemblage: a comparison of static panels and boat hulls during the boating season,” *Biofouling* **19**, 187–195 (2003).
- 555 [12] R. L. Townsin, “The ship fouling penalty,” *Biofouling* **19**, 9–15 (2003).
- 556 [13] J. Loxton, A.K. Macleod, C. R. Nall, T. McCollin, I. Machado, T. Simas, T. Vance, C. Kenny, A. Want, and R. G. Miller,  
557 “Setting an agenda for biofouling research for the marine renewable energy industry,” *International Journal of Marine  
558 Energy* **19**, 292–303 (2017).
- 559 [14] Carl C. Stringer and Brian L. Polyage, “Implications of biofouling on cross-flow turbine performance,” *SN Applied Sciences*  
560 **2**, 464 (2020).
- 561 [15] J.S. Walker, R. B. Green, E. A. Gillies, and C. Phillips, “The effect of a barnacle-shaped excrescence on the hydrodynamic  
562 performance of a tidal turbine blade section,” *Ocean Engineering* **217**, 107849 (2020).
- 563 [16] M. P. Schultz, J. A. Bendick, E. R. Holm, and W. M. Hertel, “Economic impact of biofouling on a naval surface ship,”  
564 *Biofouling* **27**, 87–98 (2011).
- 565 [17] Y. K. Demirel, O. Turan, and A. Incesik, “Predicting the effect of biofouling on ship resistance using cfd,” *Applied Ocean  
566 Research* **62**, 100–118 (2017).
- 567 [18] Y. K. Demirel, D. Uzun, Y. Zhang, H-C. Fang, A. H. Day, and O. Turan, “Effect of barnacle fouling on ship resistance  
568 and powering,” *Biofouling* **33**, 819–834 (2017).
- 569 [19] D. Uzun, Y. Zhang, Y. K. Demirel, and O. Turan, “Experimental determination of added resistance due to barnacle  
570 fouling of ships by using 3d printed barnacles,” in *5th International Conference on Advanced Measurement Technology for  
571 the Maritime Industry (AMT’17)* (University of Strathclyde, 2017).
- 572 [20] F. R. Hama, *Boundary-layer characteristics for smooth and rough surfaces* (Transactions - The Society of Naval Architects  
573 and Marine Engineers, 1954).
- 574 [21] J. A. C. Orme, I. Masters, and R. T. Griffiths, “Investigation of the effect of biofouling on the efficiency of marine current  
575 turbines,” in *MAREC 2001*, edited by C. French (Institute of Marine Engineers, 2001) pp. 91–99.
- 576 [22] Jasim Sadique, *Turbulent flows over macro-scale roughness elements - From biofouling barnacles to urban canopies*, Ph.D.  
577 thesis, John Hopkins University, Baltimore, Maryland (2016).
- 578 [23] Decheng Kong, Chaofang Dong, Zhaoran Zheng, Feixiong Mao, Aoni Xu, Xiaoqing Ni, Cheng Man, Jizheng Yao, Kui Xiao,  
579 and Xiaogang Li, “Surface monitoring for pitting evolution into uniform corrosion on cu-ni-zn ternary alloy in alkaline  
580 chloride solution: ex-situ LCM and in-situ SECM,” *Applied Surface Science* **440**, 245–257 (2018).
- 581 [24] H. Schlichting, “Experimental investigation of the problem of surface roughness,” *Ingenieur-Archiv* **7**, 1–34 (1937).
- 582 [25] O. Coceal, T. G. Thomas, and S. E. Belcher, “Spatial variability of flow statistics within regular building arrays,”  
583 *Boundary-Layer Meteorology* **125**, 537–552 (2007).
- 584 [26] S. Leonardi and I. P. Castro, “Channel flow over large cube roughness: a direct numerical simulation study,” *Journal of  
585 Fluid Mechanics* **651**, 519–539 (2010).
- 586 [27] K. A. Flack and M. P. Schultz, “Roughness effects on wall-bounded turbulent flows,” *Physics of Fluids* **26**, 101305 (2014).
- 587 [28] Yun Kyung Choi, Hyeon Gyu Hwang, Young Mo Lee, and Jae Hwa Lee, “Effects of the roughness height in turbulent  
588 boundary layers over rod- and cuboid-roughened walls,” *International Journal of Heat and Fluid Flow* **85**, 108644 (2020).
- 589 [29] Johann Nikuradse, “Laws of flow in rough pipes,” *VDI Forschungsheft* **361** (1933).
- 590 [30] R. Mejia-Alvarez and K.T. Christensen, “Low-order representations of irregular surface roughness and their impact on a  
591 turbulent boundary layer,” *Physics of Fluids* **22**, 015106 (2010).
- 592 [31] J Yuan and P Piomelli, “Estimation and prediction of the roughness function on realistic surfaces,” *Journal of Turbulence*  
593 **15**, 350–365 (2014).
- 594 [32] M. Thakkar, A. Busse, and N. D. Sandham, “Surface correlations of hydrodynamic drag for transitionally rough engineering  
595 surfaces,” *Journal of Turbulence* **18**, 138–169 (2016).
- 596 [33] P. Forooghi, A. Stroh, F. Magagnato, S. Jakirlić, and B. Frohnapfel, “Toward a universal roughness correlation,” *Journal  
597 of Fluids Engineering* **139**, 121201–121201–12 (2017).
- 598 [34] Y. Kuwata and Y. Kawaguchi, “Direct numerical simulation of turbulence over systematically varied irregular rough  
599 surfaces,” *Journal of Fluid Mechanics* **862**, 781–815 (2019).
- 600 [35] B. Nugroho, J. P. Monty, I. K. A. P. Utama, B. Ganapathisubramani, and N. Hutchins, “Non-type behaviour of roughness  
601 when in-plane wavelength approaches the boundary layer thickness,” *Journal of Fluid Mechanics* **911**, A1 (2021).
- 602 [36] F. Alves Portela, A. Busse, and N. D. Sandham, “Numerical study of fourier-filtered rough surfaces,” *Physical Review  
603 Fluids* **6**, 084606 (2021).
- 604 [37] Charles Darwin, *A monograph on the sub-class Cirripedia, with figures of all the species* (The Ray Society, 1854).

- 605 [38] E. W. Knight-Jones, “Laboratory experiments on gregariousness during setting in *Balanus balanoides* and other barnacles,”  
606 *Journal of Experimental Biology* **30**, 584–598 (1953).
- 607 [39] E.W. Knight-Jones and D.J. Crisp, “Gregariousness in barnacles in relation to the fouling of ships and to anti-fouling  
608 research,” *Nature* **171**, 1109–1110 (1953).
- 609 [40] D.J. Crisp, “The behaviour of barnacle cyprids in relation to water movement over a surface,” *Journal of Experimental*  
610 *Biology* **32**, 569–590 (1955).
- 611 [41] L.S. Mullineaux and C.A. Butman, “Initial contact, exploration and attachment of barnacle (*Balanus amphitrite*) cyprids  
612 settling in flow,” *Marine Biology* **110**, 93–103 (1991).
- 613 [42] K. C. Chaw and W. R. Birch, “Quantifying the exploratory behaviour of *Amphibalanus amphitrite* cyprids,” *Biofouling*  
614 **25** (2009).
- 615 [43] Sotirios Sarakinos and Angela Busse, “An algorithm for the generation of biofouled surfaces for application in marine  
616 hydrodynamics,” in *Progress in CFD for wind and tidal offshore turbines*, edited by Esteban Ferrer and Adeline de Montlaur  
617 (Springer, 2019).
- 618 [44] K. Pearson, “Ix. mathematical contributions to the theory of evolution. -xix. second supplement to a memoir on skew  
619 variation,” *Physical Transactions of the Royal Society A* **216**, 429–457 (1916).
- 620 [45] E. Napoli, V. Armenio, and M. De Marchis, “The effect of slope of irregularly distributed roughness elements on turbulent  
621 wall-bounded flows,” *Journal of Fluid Mechanics* **613**, 385–394 (2008).
- 622 [46] D. Chung, N. Hutchins, M. P. Schultz, and K. A. Flack, “Predicting the drag of rough surfaces,” *Annual Review of Fluid*  
623 *Mechanics* **53**, 439–471 (2021).
- 624 [47] K. M. Womack, R. J. Volino, C. Meneveau, and M. P. Schultz, “Turbulent boundary layer flow over regularly and  
625 irregularly arranged truncated cone surfaces,” *Journal of Fluid Mechanics* **933** (2022), 10.1017/jfm.2021.946.
- 626 [48] A. Busse, M. Lütznier, and N. D. Sandham, “Direct numerical simulations of turbulent flow over rough surface based on  
627 a surface scan,” *Computers & Fluids* **116**, 129–147 (2015).
- 628 [49] J. Yang and E. Balaras, “An embedded-boundary formulation for large-eddy simulation of turbulent flows interacting with  
629 moving boundaries,” *Journal of Computational Physics* **215**, 12–40 (2006).
- 630 [50] L. Chan, M. MacDonald, D. Chung, N. Hutchins, and A. Ooi, “A systematic investigation of roughness height and  
631 wavelength in turbulent pipe flow in the transitionally rough regime,” *J. Fluid Mech.* **771**, 743–777 (2015).
- 632 [51] A. Busse, M. Thakkar, and N. D. Sandham, “Reynolds-number dependence of the near-wall flow over irregular rough  
633 surfaces,” *Journal of Fluid Mechanics* **810**, 196–224 (2017).
- 634 [52] M. MacDonald, L. Chan, D. Chung, N. Hutchins, and A. Ooi, “Turbulent flow over transitionally rough surfaces with  
635 varying roughness densities,” *Journal of Fluid Mechanics* **804**, 130–161 (2016).
- 636 [53] M. P. Schultz and K. A. Flack, “Turbulent boundary layers on a systematically varied rough wall,” *Physics of Fluids* **21**,  
637 015104 (2009).
- 638 [54] J. Jiménez, “Turbulent flows over rough walls,” *Annual Review of Fluid Mechanics* **36**, 173–196 (2004).
- 639 [55] R. L. Webb, Eckert E. R. G., and Goldstein R. J., “Heat transfer and friction in tubes with repeated-rib roughness,”  
640 *International Journal of Heat and Mass Transfer* **14**, 601–617 (1971).
- 641 [56] I. Tani, “Turbulent boundary layer development over rough surfaces,” in *Perspectives in Turbulence Studies*, edited by  
642 H. U. Meier and P. Bradshaw (Spinger-Verlag, 1987) pp. 223–249.
- 643 [57] P. R. Bandyopadhyay, “Rough-wall turbulent boundary layers in the transition regime,” *Journal of Fluid Mechanics* **180**,  
644 231–266 (1987).
- 645 [58] M. Placidi and B. Ganapathisubramani, “Effects of frontal and plan solidities on aerodynamic parameters and the roughness  
646 sublayer in turbulent boundary layers,” *Journal of Fluid Mechanics* **782**, 541–566 (2015).
- 647 [59] K. A. Flack, M. P. Schultz, and J. M. Barros, “Skin friction measurements of systematically-varied roughness: Probing  
648 the role of roughness amplitude and skewness,” *Flow, Turbulence and Combustion* **104**, 317–329 (2019).
- 649 [60] W. K. George, “Is there a universal log law for turbulent wall-bounded flows?” *Philosophical Transactions of the Royal*  
650 *Society of London A* **365**, 789–806 (2007).
- 651 [61] J. J. Finnigan, “Turbulence in plant canopies,” *Annual Review of Fluid Mechanics* **32**, 519–572 (2000).
- 652 [62] A. Sharma and R. García-Mayoral, “Scaling and dynamics of turbulence over sparse canopies,” *Journal of Fluid Mechanics*  
653 **888** (2020), 10.1017/jfm.2019.999.
- 654 [63] A. Busse and N. D. Sandham, “Parametric forcing approach to rough-wall turbulent channel flow,” *Journal of Fluid*  
655 *Mechanics* **712**, 169–202 (2012).
- 656 [64] P. Foroughi, B. Frohnappfel, F. Magagnato, and A. Busse, “A modified parametric forcing approach for modelling of  
657 roughness,” *International Journal of Heat and Fluid Flow* **71**, 200–209 (2018).
- 658 [65] H. Cheng and I. P. Castro, “Near wall flow over urban-line roughness,” *Boundary-Layer Meteorology* **104**, 229–259 (2002).
- 659 [66] M. R. Raupach and R. H. Shaw, “Averaging procedures for flow within vegetation canopies,” *Boundary-Layer Meteorology*  
660 **22**, 79–90 (1982).
- 661 [67] E. Florens, O. Eiff, and F. Moulin, “Defining the roughness sublayer and its turbulence statistics,” *Experiments in Fluids*  
662 **54**, 1500–1515 (2013).
- 663 [68] A. Sharma and R. García-Mayoral, “Turbulent flows over dense filament canopies,” *Journal of Fluid Mechanics* **888** (2020),  
664 10.1017/jfm.2020.27.
- 665 [69] A. Busse and T. O. Jelly, “Influence of surface anisotropy on turbulent flow over irregular roughness,” *Flow, Turbulence*  
666 *and Combustion* **104**, 331–354 (2019).
- 667 [70] T. O. Jelly and A. Busse, “Reynolds number dependence of Reynolds and dispersive stresses in turbulent channel flow  
668 past irregular near-Gaussian roughness,” *International Journal of Heat and Fluid Flow* **80**, 108485 (2019).

- 669 [71] T. O. Jelly and A. Busse, “Reynolds and dispersive shear stress contributions above highly skewed roughness,” *Journal of*  
670 *Fluid Mechanics* **852**, 710–724 (2018).
- 671 [72] P. Forooghi, A. Stroh, P. Schlatter, and B. Frohnafel, “Direct numerical simulation of flow over dissimilar, randomly  
672 distributed roughness elements: A systematic study on the effect of surface morphology on turbulence,” *Physical Review*  
673 *Fluids* **3**, 044605 (2018).
- 674 [73] S. Trk, G. Daschiel, A. Stroh, Y. Hasegawa, and B. Frohnafel, “Turbulent flow over superhydrophobic surfaces with  
675 streamwise grooves,” *Journal of Fluid Mechanics* **747**, 186–217 (2014).
- 676 [74] R. Mejia-Alvarez and K. T. Christensen, “Wall-parallel stereo particle-image velocimetry measurements in the roughness  
677 sublayer of turbulent flow overlying highly irregular roughness,” *Physics of Fluids* **25**, 115109 (2013).
- 678 [75] J. P. Bons, R. P. Taylor, Stephen T. McClain, and R. B. Rivir, “The many faces of turbine surface roughness,” *Journal*  
679 *of Turbomachinery* **123**, 739–748 (2001).
- 680 [76] T. R. Oke, “Street design and urban canopy layer climate,” *Energy and Buildings* **11**, 103–113 (1988).